A fictitious domain method with enhanced interfacial mass conservation for immersed FSI with thin-walled solids

Daniele Corti, Jérôme Diaz, Marina Vidrascu, Dominique Chapelle, Philippe Moireau, Miguel Angel Fernández

To cite this version:

Daniele Corti, Jérôme Diaz, Marina Vidrascu, Dominique Chapelle, Philippe Moireau, et al.. A fictitious domain method with enhanced interfacial mass conservation for immersed FSI with thin-walled solids. 2024. hal-04713023

HAL Id: hal-04713023
https://hal.science/hal-04713023v1

Preprint submitted on 28 Sep 2024

A fictitious domain method with enhanced interfacial mass conservation for immersed FSI with thin-walled solids

Daniele C. Corti[a], Jérôme Diaz[b], Marina Vidrascu[a], Dominique Chapelle[b], Philippe Moireau[b] and Miguel A. Fernández[a]

[a]Sorbonne Université & CNRS, UMR 7598 LJLL – Inria, Paris, France
[b]Inria, LMS - CNRS - Ecole Polytechnique, Institut Polytechnique de Paris, Palaiseau France

ARTICLE INFO

Keywords:
Fluid structure interaction
Fictitious domain
3D-shell
Interfacial mass conservation.

ABSTRACT

In this paper, we extend the low-order fictitious domain method with enhanced mass conservation presented in *[ESAIM: Math. Model. Numer. Anal., 58(1):303–333, 2024.]* to the case of coupling with immersed thin-walled solids. Both surface and 3D-shell models are considered for the description of the solid, including contact between solids. For both models, the interface coupling is enforced on the mid-surface of the shell using a stabilized Lagrange multiplier formulation. Numerical examples in both two and three dimensions illustrate the effectiveness of the method, including its successful application to the simulation of aortic heart valve dynamics.

1. Introduction

The numerical simulation of mechanical interactions between incompressible viscous fluids and immersed moving thin-walled structures plays a fundamental role in a wide variety of engineering fields, ranging from the biomechanics of heart valves to the aeroelasticity of parachutes (see, e.g., [47, 66, 51, 69, 62]). One of the fundamental challenges encountered in the approximation of these systems is the introduction of weak and strong discontinuities in the fluid velocity and pressure fields, respectively, induced by the immersed thin-walled nature of the solid. Preserving these properties at the discrete level is known to play an essential role in the accuracy of the resulting numerical method. In particular, pressure discontinuities across the interface are crucial for ensuring interfacial mass conservation, while discontinuities in the velocity gradient are necessary for achieving optimal accuracy.

Extensive research has been conducted in the development of numerical methods for fluid-structure interaction (FSI), resulting in a wide range of methodologies typically classified as fitted (conforming) or unfitted (non-conforming) mesh methods. In fitted mesh methods, the fluid and structure meshes match at their interface, with the fluid problem typically solved on a deforming mesh that follows the motion of the interface. This facilitates the enforcement of interface conditions, and (weak and strong) discontinuities in the solution can be straightforwardly incorporated at the discrete level, resulting in an optimally accurate method. Noteworthy examples of such methods include those employing the Arbitrary Lagrangian-Eulerian (ALE) formulation in the fluid (see, e.g., [27, 52, 29, 60, 64, 43]) and unified continuum modeling for FSI (see [39, 40, 46]). Nevertheless, the body-fitted nature of the mesh presents challenges whenever the solid undergoes large deflections, particularly in cases of contact between solids, leading to highly distorted fluid meshes that may necessitate remeshing or topological modifications (see, for instance, [2, 63]), thereby increasing computational costs.

Unfitted mesh methods are a widespread approach to avoid these issues. In this class of methods, the fluid and solid meshes are non-conforming at the interface, allowing the solid mesh to freely move over the background fluid mesh. However, this flexibility comes at the cost of potentially encountering accuracy issues due to the lack of proper interfacial representation within the fluid computational mesh. Notable methods in this category include the Immersed Boundary (IBM) and Immersed Finite Element (IFEM) methods (see, e.g., [53, 71, 49, 11, 68]), where the solid acts as an external body force in the fluid equations, and the Fictitious Domain (FD) methods (see, e.g., [59, 4, 25, 3, 13, 41, 12, 14]), where the kinematic constraint is imposed via Lagrange multipliers or penalization.

---

*Corresponding author: Miguel A. Fernández

daniele.corti@inria.fr (D.C. Corti); jerome.diaz@inria.fr (J. Diaz); marina.vidrascu@inria.fr (M. Vidrascu); dominique.chapelle@inria.fr (D. Chapelle); philippe.moireau@inria.fr (P. Moireau); miguel.fernandez@inria.fr (M.A. Fernández)
ORCID(s):

These methods often suffer from spatial inaccuracies due to discrete treatment of interface conditions and limitations in accommodating discontinuities across the interface (see, e.g., [54, 34, 41, 61, 14, 19]). Although mesh adaptivity can mitigate some issues, it does not fully resolve the problem (see, e.g., [36, 6]).

One approach to enhance interfacial mass conservation involves using discontinuous pressure approximations with higher-order polynomials for velocities (see, e.g., [4, 10, 9, 13]) or employing divergence-free velocity approximations (see [19]). Cut-FEM methods ensure high accuracy by integrating equations solely in the physical region and incorporating stabilizing terms for robustness, but they require intricate computer implementation due to precise tracking of interface intersections and quadrature over arbitrary polygons (see, e.g., [35, 37, 15]). The extended-FEM (XFEM) method, combining cut-FEM with local enrichment, addresses some challenges but introduces additional unknowns (Lagrange multipliers) and potential ill-conditioning (see, e.g., [72, 31, 58]). The Nitsche-XFEM method overcomes these difficulties by combining overlapping meshes with Nitsche's approach to interface coupling and suitable stabilization in the interfacial zone for robustness (see [1, 17, 73]). However, the superior accuracy of the Nitsche-FEM approach comes with increased computational complexity, requiring a more intricate computer implementation and specific tracking of mesh intersections (see, e.g., [1]). It is also worth mentioning the recent cut-FEM method reported in [16] based on the minimal divergence-free element introduced in [23].

An alternative approach to enhance interfacial mass conservation consists in boosting the incompressibility constraint through grad-div penalization in the interfacial zone, although this is known to yield severe ill-conditioning issues (see, e.g., [41, 30, 18, 14]).

In this work, we address the mass conservation challenges inherent in standard fictitious domain methods by employing the low-order fictitious domain method introduced in [24]. This approach enhances mass conservation across the interface by imposing a single global velocity constraint on one side of the interface using a scalar Lagrange multiplier. This constraint can be alternatively viewed as an enrichment of the pressure discrete space with a single discontinuous basis function. We extend the application of this method to a fluid-structure interaction framework for thin-walled structures, validating its effectiveness through an extensive set of 2D and 3D numerical examples. Two distinct modeling options are considered for the description of the thin-walled solid dynamics: the 2D-shell model under Reissner-Mindlin assumptions (see, e.g., [5, 8, 21]) and the 3D-shell model (introduced in [22]). The 3D-shell model offers significant advantages, enabling the use of general 3D constitutive relations within the shell framework and facilitating natural displacement-based coupling with other 3D media. We present a coupling modeling framework in which the interface conditions are enforced on the mid-surface of the solid for both 2D and 3D-shell models. Besides its simplicity, in the case of the 3D-shell, this approach avoids the issues associated with managing the fictitious region corresponding to the solid within the fluid.

The rest of the paper is organized as follows. The continuous setting is outlined in Section 2, where the coupling with the two different shell models is presented within a common framework. Section 3 describes the proposed fictitious domain approximation with enhanced mass conservation. Section 4 presents a comprehensive set of numerical examples. In particular, in Section 4.1, the proposed method is compared to other fitted and unfitted mesh methods in three 2D benchmarks. Section 4.2 is dedicated to the comparison of the two shell models proposed, while Section 4.3 combines the proposed FSI method with a penalty-based contact algorithm for shell structures, allowing the FSI simulation of an aortic heart valve in a realistic setting. Finally, a summary of the main conclusions is given in Section 5.

2. Problem setting

Let $\Omega \subset \mathbb{R}^d$, where $d = 2$ or 3, be a given fixed domain whose boundary is denoted by $\partial\Omega$. We consider a fluid-structure interaction problem in Ω, involving a thin-walled structure immersed in a viscous, incompressible Newtonian fluid. At time t, the fluid and structure domains are denoted as $\Omega^{\mathrm{f}}(t)$ and $\Omega^{\mathrm{s}}(t)$, respectively. The reference configuration of the structure is denoted by Ω^{s}. The mid-surface of Ω^{s}, denoted by Σ, is assumed to be an oriented manifold of co-dimension 1, with a unit normal vector $\boldsymbol{n}_\Sigma$. The current position of the structure mid-surface $\Sigma(t)$ is described in terms of the deformation map $\boldsymbol{\psi} : \Sigma \times \mathbb{R}^+ \to \mathbb{R}^d$ as $\Sigma(t) = \boldsymbol{\psi}(\Sigma, t)$. In what follows, we shall use the notation $\boldsymbol{\psi}_t \overset{\mathrm{def}}{=} \boldsymbol{\psi}(\cdot, t)$.

The fluid-structure interface is given by the structure mid-surface $\Sigma(t)$, neglecting the shell thickness the interface coupling. This assumption is a widely used modeling simplification in contexts involving the coupling of surface-based thin-walled models to 3D-based models (see, e.g., [20]). We hereby extend this approach to the case of the coupling with 3D-shell models. Consequently, the fluid domain evolves over time according to the deformation of the solid mid-surface as $\Omega^{\mathrm{f}}(t) \overset{\mathrm{def}}{=} \Omega \backslash \Sigma(t) \subset \mathbb{R}^d$, with boundary $\partial\Omega^{\mathrm{f}}(t) = \Sigma(t) \cup \partial\Omega$. In the sequel, we consider two modeling

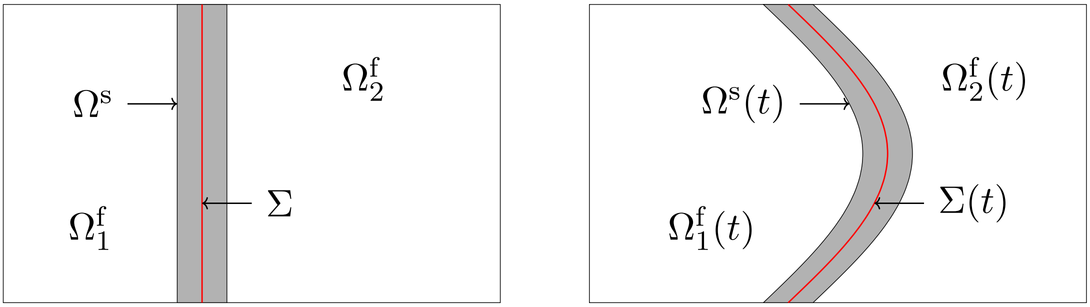

(a) Reference configuration.

(b) Current configuration at time t.

Figure 1: Example of a structure represented by the domain $\Omega^{\mathrm s}$, with its mid-surface Σ.

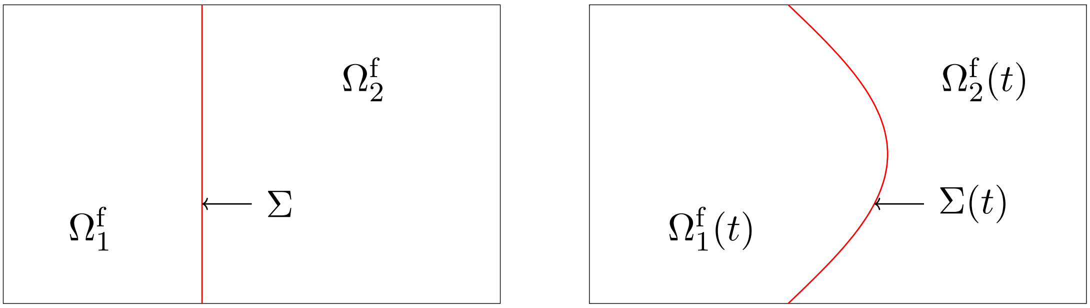

(a) Reference configuration.

(b) Current configuration at time t.

Figure 2: Example of a structure represented by its mid-surface Σ.

approaches: one with the solid domain represented by $\Omega^{\mathrm s}$ (see Figure 1), and another where the solid is represented by its mid-surface Σ (see Figure 2). Nevertheless, in both cases the fluid domain only sees the solid mid-surface.

Let us consider the following partition of the boundaries $\partial\Omega^{\mathrm f}(t) = \Gamma^{\mathrm f}_{\mathrm D}\cup\Gamma^{\mathrm f}_{\mathrm N}\cup\Sigma(t)$, $\partial\Omega^{\mathrm s} = \Gamma^{\mathrm s}_{\mathrm D}\cup\Gamma^{\mathrm s}_{\mathrm N}$ and $\partial\Sigma\cap\Gamma^{\mathrm s}_{\mathrm D} = \partial\Sigma$, with the subscript D (resp. N) meaning the boundary portion on which Dirichlet (resp. Neumann) condition is enforced. Moreover, assuming that the structure mid-surface $\Sigma(t)$ divides the fluid domain $\Omega^{\mathrm f}(t)$ into two subdomains $\Omega^{\mathrm f}_1(t)$ and $\Omega^{\mathrm f}_2(t)$, such that $\Omega^{\mathrm f}_1(t)\cap\Omega^{\mathrm f}_2(t) = \emptyset$, $\partial\Omega^{\mathrm f}_1(t)\cap\partial\Omega^{\mathrm f}_2(t) = \Sigma(t)$ and, for $i = 1, 2$, $\Gamma^{\mathrm f}_{\mathrm N}\cap\partial\Omega^{\mathrm f}_i(t) \neq \emptyset$, we define $\boldsymbol{n}_1 \overset{\text{def}}{=} \boldsymbol{n}_\Sigma \overset{\text{def}}{=} -\boldsymbol{n}_2$ over $\Sigma(t)$ and $\boldsymbol{n}_i \overset{\text{def}}{=} \boldsymbol{n}$, with $i = 1, 2$, on $\partial\Omega^{\mathrm f}_i(t)\setminus\Sigma(t)$. For a given continuous scalar or tensorial field ϕ defined in $\Omega^{\mathrm f}(t)$, possibly discontinuous across $\Sigma(t)$, we define its sided restrictions, noted by ϕ_1 and ϕ_2, as

$$\phi_1(\boldsymbol{x}) \overset{\text{def}}{=} \lim_{\delta\to 0^-} \phi(\boldsymbol{x} + \delta\boldsymbol{n}_1) \quad \phi_2(\boldsymbol{x}) \overset{\text{def}}{=} \lim_{\delta\to 0^-} \phi(\boldsymbol{x} + \delta\boldsymbol{n}_2) \qquad \forall\boldsymbol{x}\in\Sigma(t).$$

We also define the following jump operators across the interface $\Sigma(t)$:

$$[\![\phi]\!] \overset{\text{def}}{=} \phi_1 - \phi_2, \quad [\![\phi\boldsymbol{n}]\!] \overset{\text{def}}{=} \phi_1\boldsymbol{n}_1 + \phi_2\boldsymbol{n}_2.$$

2.1. Coupled fluid-structure interaction problems

In this section, we introduce two distinct FSI problems that differ in the model used to describe the dynamics of the solid.

2.1.1. Coupling with a 3D-shell model

For the first fluid-structure interaction model, we consider the Navier-Stokes equations for homogeneous, incompressible, and Newtonian fluids, along with a nonlinear 3D-shell model to describe the behavior of the structure. The coupled problem under consideration is formulated as follows: For all $t \in \mathbb{R}^+$, find the fluid velocity and pressure $\boldsymbol{u} : \Omega\times\mathbb{R}^+ \to \mathbb{R}^3$, $p : \Omega\times\mathbb{R}^+ \to \mathbb{R}$, the structure displacement and velocity $\boldsymbol{d} : \Omega^{\mathrm s}\times\mathbb{R}^+ \to \mathbb{R}^3$, $\boldsymbol{u}^{\mathrm s} : \Omega^{\mathrm s}\times\mathbb{R}^+ \to \mathbb{R}^3$

such that

$$\begin{cases} \rho^{\mathrm{f}} \partial_t \boldsymbol{u} + \rho^{\mathrm{f}} (\boldsymbol{u} \cdot \nabla \boldsymbol{u}) - \boldsymbol{\nabla} \cdot \boldsymbol{\sigma}^{\mathrm{f}}(\boldsymbol{u}, p) = \boldsymbol{0} & \text{in} \quad \Omega^{\mathrm{f}}(t), \\ \nabla \cdot \boldsymbol{u} = 0 & \text{in} \quad \Omega^{\mathrm{f}}(t), \\ \boldsymbol{u} = \boldsymbol{0} & \text{on} \quad \Gamma^{\mathrm{f}}_{\mathrm{D}}, \\ \boldsymbol{\sigma}^{\mathrm{f}}(\boldsymbol{u}, p)\boldsymbol{n} = \boldsymbol{0} & \text{on} \quad \Gamma^{\mathrm{f}}_{\mathrm{N}}, \end{cases} \tag{1}$$

$$\begin{cases} \rho^{\mathrm{s}} \partial_t \boldsymbol{u}^{\mathrm{s}} + \boldsymbol{\nabla} \cdot \boldsymbol{\sigma}^{\mathrm{s}}(\boldsymbol{d}) = \delta_\Sigma \boldsymbol{T} & \text{in} \quad \Omega^{\mathrm{s}}, \\ \boldsymbol{u}^{\mathrm{s}} = \partial_t \boldsymbol{d} & \text{on} \quad \Omega^{\mathrm{s}}, \\ \boldsymbol{d} = \boldsymbol{0} & \text{on} \quad \Gamma^{\mathrm{s}}_{\mathrm{D}}, \\ \boldsymbol{\sigma}^{\mathrm{s}}(\boldsymbol{d})\boldsymbol{n} = \boldsymbol{0} & \text{on} \quad \Gamma^{\mathrm{s}}_{\mathrm{N}}, \end{cases} \tag{2}$$

$$\begin{cases} \boldsymbol{\psi} = \boldsymbol{I}_\Sigma + \boldsymbol{d} \quad \text{on} \quad \Sigma, \quad \Sigma(t) = \boldsymbol{\psi}_t(\Sigma), \quad \Omega^{\mathrm{f}}(t) = \Omega \backslash \Sigma(t), \\ \boldsymbol{u} = \boldsymbol{u}^{\mathrm{s}} \circ \boldsymbol{\psi}_t^{-1} \quad \text{on} \quad \Sigma(t), \\ \displaystyle\int_\Sigma \boldsymbol{T} \cdot \boldsymbol{w} = - \int_{\Sigma(t)} [\![\boldsymbol{\sigma}^{\mathrm{f}}(\boldsymbol{u}, p)\boldsymbol{n}]\!] \cdot \boldsymbol{w} \circ \boldsymbol{\psi}_t^{-1} \quad \forall\, \boldsymbol{w} \in \boldsymbol{W}. \end{cases} \tag{3}$$

The symbols ρ^{f} and ρ^{s} represent the fluid and solid densities, respectively. δ_Σ denotes the Dirac surface measure supported on Σ. The fluid Cauchy stress tensor is given by

$$\boldsymbol{\sigma}^{\mathrm{f}}(\boldsymbol{u}, p) \stackrel{\text{def}}{=} 2\mu \boldsymbol{\varepsilon}(\boldsymbol{u}) - p\boldsymbol{I},$$

where μ denotes the fluid dynamic viscosity, and the strain rate tensor $\boldsymbol{\varepsilon}(\boldsymbol{u})$ is defined as

$$\boldsymbol{\varepsilon}(\boldsymbol{u}) \stackrel{\text{def}}{=} \frac{1}{2}\big(\boldsymbol{\nabla}\boldsymbol{u} + \boldsymbol{\nabla}\boldsymbol{u}^{\mathrm{T}}\big).$$

The first Piola–Kirchhoff stress tensor of the structure $\boldsymbol{\sigma}^{\mathrm{s}}(\boldsymbol{d})$ is assumed to be given in terms of $\boldsymbol{d}$ via an appropriate constitutive law. The relations in (3) respectively enforce the geometrical compatibility, the kinematic and the dynamic coupling at the interface between the fluid and the solid media. Here, the symbol $\boldsymbol{W}$ stands for the space of the traces on Σ of admissible solid displacements, and $\boldsymbol{T}$ represents the fluid traction acting on the reference configuration of the interface.

2.1.2. Coupling with a 2D-shell model

In the second fluid-structure interaction model, we consider a nonlinear elastic model for 2D-shell structures. In this framework, the resulting coupled fluid-structure problem is stated as follows: Find the fluid velocity and pressure $\boldsymbol{u} : \Omega \times \mathbb{R}^+ \to \mathbb{R}^d$, $p : \Omega \times \mathbb{R}^+ \to \mathbb{R}$, the solid displacement and velocity $\boldsymbol{d} : \Sigma \times \mathbb{R}^+ \to \mathbb{R}^d$, $\boldsymbol{u}^{\mathrm{s}} : \Sigma \times \mathbb{R}^+ \to \mathbb{R}^d$ such that, for all $t \in \mathbb{R}^+$, equations (1), (3) are satisfied, and

$$\begin{cases} \rho^{\mathrm{s}} \epsilon \partial_t \boldsymbol{u}^{\mathrm{s}} + \boldsymbol{L}(\boldsymbol{d}) = \boldsymbol{T} & \text{on} \quad \Sigma, \\ \boldsymbol{u}^{\mathrm{s}} = \partial_t \boldsymbol{d} & \text{on} \quad \Sigma, \\ \boldsymbol{d} = \boldsymbol{0} & \text{on} \quad \partial\Sigma. \end{cases} \tag{4}$$

Here, the nonlinear surface operator $\boldsymbol{L}$ describes the elastic behavior of the structure. It's worth noting that the Dirac measure is absent from the right-hand side of $(4)_1$, as this relation is enforced directly on Σ.

2.1.3. Contact model

In the present study, we consider a non-penetrating contact condition as in [50]. However, we choose here to solve the contact problem as part of the solid formulation, using a penalization method, with a penalization energy given by

$$\mathcal{W}_{\text{contact}} \stackrel{\text{def}}{=} \int_{\Sigma(t)} \frac{\kappa_{\mathrm{c}}}{2} \Big| \operatorname{dist}(\boldsymbol{x}, \Sigma(t)) \Big|_-^2, \tag{5}$$

where $\Sigma(t)$ is the self-contact surface of interest for the point considered.

Then we have to compute the gradient of the distance with respect to the displacement field. The difficulty is that we must calculate the distance to a surface that moves according to the deformation. Therefore, introducing the projection operator $\pi_{\Sigma(t)}$ on $\Sigma(t)$ as in [50], we have

$$\begin{aligned}\boldsymbol{\nabla}_{\boldsymbol{d}}\operatorname{dist}(\boldsymbol{x},\Sigma(t))\cdot\boldsymbol{\delta} &= -\boldsymbol{\nabla}_{\boldsymbol{d}}\big((\pi_{\Sigma(t)}(\boldsymbol{x})-\boldsymbol{x})\cdot\boldsymbol{n}_{\Sigma(t)}(\pi_{\Sigma(t)}(\boldsymbol{x}))\big)\cdot\boldsymbol{\delta}\\ &= \big(\boldsymbol{\nabla}_{\boldsymbol{d}}\boldsymbol{x}\cdot\boldsymbol{\delta}\big)\cdot\boldsymbol{n}_{\Sigma(t)} - \big(\boldsymbol{\nabla}_{\boldsymbol{d}}\pi_{\Sigma(t)}(\boldsymbol{x})\cdot\boldsymbol{\delta}\big)\cdot\boldsymbol{n}_{\Sigma(t)} + \big(\boldsymbol{\nabla}_{\boldsymbol{d}}\boldsymbol{n}_{\Sigma(t)}\cdot\boldsymbol{\delta}\big)\cdot(\pi_{\Sigma(t)}(\boldsymbol{x})-\boldsymbol{x}))\\ &= \boldsymbol{n}_{\Sigma(t)}(\pi_{\Sigma(t)}(\boldsymbol{x}))\cdot\big(\boldsymbol{\delta}(\boldsymbol{x})-\boldsymbol{\delta}(\pi_{\Sigma(t)}(\boldsymbol{x}))\big).\end{aligned}$$

Therefore, the variational terms associated with the constraint (5) is

$$a_{\text{contact}}(\boldsymbol{d};\boldsymbol{w}) \overset{\text{def}}{=} \int_{\Sigma(t)} \kappa_{\text{c}}\Big|\operatorname{dist}(\boldsymbol{x},\Sigma(t))\Big|_{-}\boldsymbol{n}_{\Sigma(t)}(\pi_{\Sigma(t)}(\boldsymbol{x}))\cdot\big(\boldsymbol{w}(\boldsymbol{x})-\boldsymbol{w}(\pi_{\Sigma(t)}(\boldsymbol{x}))\big), \tag{6}$$

to be included in the solid weak form $a^{\text{s}}_{\Omega^{\text{s}}}$.

From a computational implementation standpoint, a relaxed contact formulation is adopted to prevent penetration between the valve leaflets. Therefore, the distance term $\operatorname{dist}(\boldsymbol{x},\Sigma_{\text{c}}(t))$ within the contact operator (6) is replaced with the relaxed distance term $\operatorname{dist}_{\varepsilon_{\text{g}}} \overset{\text{def}}{=} \operatorname{dist}(\boldsymbol{x},\Sigma_{\text{c}}(t))-\varepsilon_{\text{g}}$, where $\varepsilon_{\text{g}} > 0$ represents a small user-defined value known as contact relaxation parameter.

2.2. Variational formulation

In the following, the closed space $H^1_\gamma(\omega)$, denotes the space of $H^1(\omega)$ functions with zero trace on $\gamma \subset \partial\Omega$, and the notation $(\cdot,\cdot)_\omega$ stands for the usual $L^2(\omega)$ scalar product. The two coupled problems introduced above (i.e., (1)–(3) and (1), (4), (3)) can be cast into a single variational formulation which treats the kinematic and dynamic coupling in a weak fashion by using Lagrange multipliers. Hence, we introduce the following functional spaces for velocity, pressure and Lagrange multiplier

$$\boldsymbol{V} \overset{\text{def}}{=} [H^1_{\Gamma^{\text{f}}_{\text{D}}}(\Omega)]^d, \qquad Q \overset{\text{def}}{=} L^2(\Omega), \qquad \boldsymbol{\Lambda} \overset{\text{def}}{=} [L^2(\Sigma)]^d,$$

the operator $a^{\text{f}} : \boldsymbol{V}\times\big(\boldsymbol{V}\times Q\big)\times\big(\boldsymbol{V}\times Q\big)\to\mathbb{R}$ given by

$$a^{\text{f}}\big(\boldsymbol{z};(\boldsymbol{u},p),(\boldsymbol{v},q)\big) \overset{\text{def}}{=} \rho^{\text{f}}(\boldsymbol{z}\cdot\nabla\boldsymbol{u},\boldsymbol{v})_\Omega + 2\mu(\boldsymbol{\varepsilon}(\boldsymbol{u}),\boldsymbol{\varepsilon}(\boldsymbol{v}))_\Omega - (p,\nabla\cdot\boldsymbol{v})_\Omega + (q,\nabla\cdot\boldsymbol{u})_\Omega, \tag{7}$$

and the bilinear form $b : \boldsymbol{\Lambda}\times\boldsymbol{\Lambda}\to\mathbb{R}$ is defined as

$$b(\boldsymbol{\mu},\boldsymbol{\xi}) \overset{\text{def}}{=} \big(\boldsymbol{\mu},\boldsymbol{\xi}\big)_\Sigma.$$

The solid operator $a^{\text{s}} : \boldsymbol{W}\times\boldsymbol{W}\to\mathbb{R}$ represents the weak form of either the first Piola-Kirchhoff stress tensor $\boldsymbol{\sigma}^{\text{s}}(\boldsymbol{d})$ (see (2)) or the abstract solid elastic operator $\boldsymbol{L}(\boldsymbol{d})$ (see (4)) depending on the structural model being considered. Noticing that $a^{\text{s}}(\boldsymbol{d};\boldsymbol{w})$ is assumed to be linear only with respect to the second argument. Similarly, the scalar product $\big(\eta,\nu\big)_{\text{s}}$ is defined based on the considered model:

$$\big(\eta,\nu\big)_{\text{s}} \overset{\text{def}}{=} \begin{cases}\big(\eta,\nu\big)_{\Omega^{\text{s}}} & \text{for the 3D-shell model (2),}\\ \epsilon\big(\eta,\nu\big)_\Sigma & \text{for the 2D-shell model (4).}\end{cases}$$

The resulting weak formulation reads as follows: For $t > 0$, find $\big(\boldsymbol{u},p,\lambda,\boldsymbol{d}\big)\in\boldsymbol{V}\times Q\times\boldsymbol{\Lambda}\times\boldsymbol{W}$, with $\boldsymbol{u}^{\text{s}} = \partial_t\boldsymbol{d}$, such that

$$\rho^{\text{f}}\big(\partial_t\boldsymbol{u},\boldsymbol{v}\big)_\Omega + a^{\text{f}}\big(\boldsymbol{u};(\boldsymbol{u},p),(\boldsymbol{v},q)\big) + \rho^{\text{s}}\big(\partial_t\boldsymbol{u}^{\text{s}},\boldsymbol{w}\big)_{\text{s}} + a^{\text{s}}\big(\boldsymbol{d};\boldsymbol{w}\big) - b\big(\lambda,\boldsymbol{v}\circ\boldsymbol{\psi}_t-\boldsymbol{w}\big) + b\big(\xi,\boldsymbol{u}\circ\boldsymbol{\psi}_t-\boldsymbol{u}^{\text{s}}\big) = 0 \tag{8}$$

for all $(\boldsymbol{v},q,\boldsymbol{\xi},\boldsymbol{w})\in\boldsymbol{V}\times Q\times\boldsymbol{\Lambda}\times\boldsymbol{W}$. Using a standard argument of integration by parts in $\Omega^{\text{f}}(t)$, it can be shown that problem (8) is equivalent to the above strong formulations with $\boldsymbol{\lambda} = -\boldsymbol{T}$ on Σ.

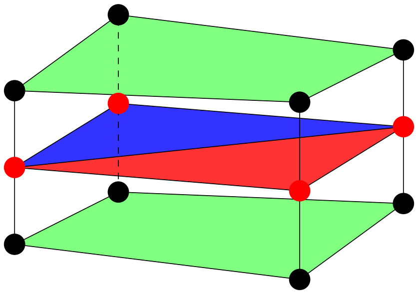

Figure 3: Example of the elements composing $\mathcal{T}_\mathcal{H}^\Sigma$ (red and blue triangles), and $\mathcal{T}_\mathcal{H}^{\Omega^{\rm s}}$ (green hexahedra).

3. Numerical approximation

In the following, $\mathcal{T}_h^\omega$ denotes a quasi-uniform triangulation of ω with a mesh parameter $h = \max_{K\in\mathcal{T}_h^\omega} h_K$, where h_K represents the diameter of the element $K \in \mathcal{T}_h^\omega$. The families of triangulations defined over Ω, $\Omega^{\rm s}$, and Σ, assumed to be polyhedral or polygonal domains, are denoted by $\{\mathcal{T}_h^\Omega\}_{0<h<1}$, $\{\mathcal{T}_\mathcal{H}^{\Omega^{\rm s}}\}_{0<\mathcal{H}<1}$, and $\{\mathcal{T}_\mathcal{H}^\Sigma\}_{0<\mathcal{H}<1}$, respectively. Note that the mesh parameters h and $\mathcal{H}$ for the fluid and solid meshes, respectively, may differ a priori. In particular, for the 3D-shell case, we assume an initial triangulation of Σ, denoted $\mathcal{T}_\mathcal{H}^{\rm q}$, consisting of quadrilaterals. The triangulation $\mathcal{T}_\mathcal{H}^\Sigma$ is derived by subdividing each element of $\mathcal{T}_\mathcal{H}^{\rm q}$ into two triangular elements. Subsequently, the triangulation $\mathcal{T}_\mathcal{H}^{\Omega^{\rm s}}$ is obtained by extruding $\mathcal{T}_\mathcal{H}^{\rm q}$ along the normal component. As a result of this construction, the mid-surface of $\mathcal{T}_\mathcal{H}^{\Omega^{\rm s}}$ is fitted to $\mathcal{T}_\mathcal{H}^\Sigma$ (see Figure 3). Alternatively, for the 2D-shell case, the triangulation $\mathcal{T}_\mathcal{H}^\Sigma$ is directly obtained by subdividing Σ into simplicials. The symbol $\tau > 0$ represents the time-step length, where $t_n \overset{\text{def}}{=} n\tau$, with $n \in \mathbb{N}$ and $\partial_\tau x^n \overset{\text{def}}{=} \big(x^n - x^{n-1}\big)/\tau$ denoting the first-order backward difference in time. Additionally, for each $n \in \mathbb{N}$, $\boldsymbol{\psi}^n \overset{\text{def}}{=} \boldsymbol{\psi}(t_n)$, $\Sigma^n \overset{\text{def}}{=} \Sigma(t_n)$, and the i-th fluid subdomain $\Omega_i^n \overset{\text{def}}{=} \Omega_i^{\rm f}(t_n)$, where $i = 1, 2$. As regards the time discretization of the fluid and solid sub-problems (1), (2) and (4), we consider second-order Newmark in the solid and a backward Euler method in the fluid.

3.1. Discrete fluid problem

The approximation of the fluid-subproblem is based on the enhanced mass conservation approach proposed and analyzed in [24]. To this purpose, we consider the following standard spaces of continuous piecewise affine functions:

$$X_h^{\rm f} \overset{\text{def}}{=} \left\{ \chi_h \in C^0(\overline{\Omega}) \middle|\, \chi_h|_K \in \mathbb{P}_1(K), \quad \forall K \in \mathcal{T}_h^\Omega \right\}, \quad X_\mathcal{H}^\Sigma \overset{\text{def}}{=} \left\{ \chi_\mathcal{H} \in C^0(\overline{\Sigma}) \middle|\, \chi_\mathcal{H}|_K \in \mathbb{P}_1(K), \quad \forall K \in \mathcal{T}_\mathcal{H}^\Sigma \right\}.$$

Finally, we introduce the discrete space $\widetilde{Q}_h \overset{\text{def}}{=} X_h^{\rm f} \subset Q$ and the discrete spaces $\boldsymbol{V}_h, Q_h^n, \boldsymbol{\Lambda}_\mathcal{H}$ for the approximation of the velocity, pressure and Lagrange multiplier as follows:

$$\boldsymbol{V}_h \overset{\text{def}}{=} [X_h^{\rm f}]^d \cap \boldsymbol{V}, \quad Q_h^n \overset{\text{def}}{=} \widetilde{Q}_h \oplus \langle 1_{\Omega_1^n} \rangle \subset Q, \quad \boldsymbol{\Lambda}_\mathcal{H} \overset{\text{def}}{=} [X_\mathcal{H}^\Sigma]^d \subset \boldsymbol{\Lambda}, \tag{9}$$

where the symbol $1_{\Omega_1^n}$ denotes the characteristic function of Ω_1^n and $\langle 1_{\Omega_1^n} \rangle$ the vector space spanned by $1_{\Omega_1^n}$. Notice that the choice of Ω_1^n and Ω_2^n is arbitrary, so that the characteristic function could have been taken over Ω_2^n instead of over Ω_1^n.

In the case of an open configuration, the separation between the two sub-domains Ω_1^n and Ω_2^n is missing. To address this issue, we propose the addition of a fictitious interface $\Sigma_{\rm fic}^n$, closing Σ^n, as illustrated in Figure 4. The purpose of $\Sigma_{\rm fic}^n$ is solely to facilitate the definition of Ω_1^n. Since no unknowns are defined on $\Sigma_{\rm fic}^n$, its selection depends solely on the specific geometry. A detailed explanation regarding the choice and construction of the fictitious interface is provided for each numerical example in Section 4. As remarked in [24], the additional global basis function in Q_h^n can be interpreted as the Lagrange multiplier associated with the additional mass conservation constraint on Ω_1^n.

Owing to the definition of the discrete pressure space (9), every $q_h \in Q_h^n$ can be decomposed into the sum of two contributions, namely,

$$q_h = \widetilde{q}_h + \widehat{q}_h, \tag{10}$$

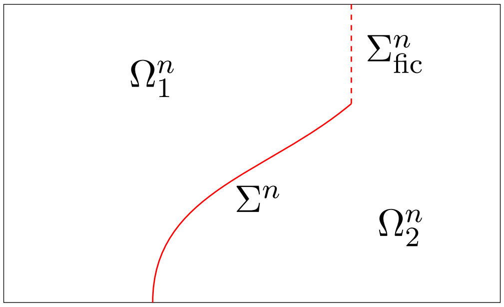

Figure 4: Example of an open configuration.

where $\widetilde{q}_h \in \widetilde{Q}_h$ is a continuous piecewise affine function over the whole computational domain Ω and $\widehat{q}_h \in \langle 1_{\Omega_1^n} \rangle$ is a Heaviside function that allows strong discontinuities across the interface Σ^n. Moreover, the following relations hold

$$\widehat{q}_h = \llbracket q_h \rrbracket 1_{\Omega_1^n}, \quad \widetilde{q}_h = q_h - \llbracket q_h \rrbracket 1_{\Omega_1^n}, \tag{11}$$

where $\llbracket q_h \rrbracket$ is the constant jump of q_h across Σ^n.

The SUPG–PSPG stabilization $s_h^{\mathrm{SP},n}$, employed to overcome the lack of inf-sup compatibility between the velocity and pressure spaces $\boldsymbol{V}_h$ and Q_h, and to guarantee robustness for high local Reynolds numbers, is given by

$$s_h^{\mathrm{SP}}\big(\boldsymbol{z}_h; (\boldsymbol{u}_h, p_h), (\boldsymbol{v}_h, q_h)\big) \overset{\text{def}}{=} \sum_{K \in \mathcal{T}_h^{\Omega}} \delta_h \big(\rho^{\mathrm{f}} (\boldsymbol{z}_h \cdot \nabla) \boldsymbol{u}_h + \nabla \widetilde{p}_h, \rho^{\mathrm{f}} (\boldsymbol{z}_h \cdot \nabla) \boldsymbol{v}_h + \nabla \widetilde{q}_h \big)_K, \tag{12}$$

where $\delta_h > 0$ a user-defined dimensionless parameter (see, e.g., [65]). Note that the above stabilization operator only acts on the continuous part, $\widetilde{p}_h$, of the discrete pressure, $p_h \in Q_h$. Finally, considering (7) and the above stabilization, the fluid discrete form reads

$$a_h^{\mathrm{f}}\big(\boldsymbol{z}_h; (\boldsymbol{u}_h, p_h), (\boldsymbol{v}_h, q_h)\big) \overset{\text{def}}{=} a^{\mathrm{f}}\big(\boldsymbol{z}_h; (\boldsymbol{u}_h, p_h), (\boldsymbol{v}_h, q_h)\big) + \frac{\rho^{\mathrm{f}}}{2} \big((\nabla \cdot \boldsymbol{z}_h)\boldsymbol{u}_h, \boldsymbol{v}_h\big)_{\Omega^{\mathrm{f}}} + s_h^{\mathrm{SP}}\big(\boldsymbol{z}_h; (\boldsymbol{u}_h, p_h), (\boldsymbol{v}_h, q_h)\big).$$

In order to overcome the instability of the saddle-point problem posed by the choice of the Lagrange multiplier finite element space $\boldsymbol{\Lambda}_{\mathcal{H}}$ in (9) and to avoid any constraint on the ratio between the fluid mesh size h and the interface mesh size $\mathcal{H}$ (as in [12]), we introduce the following stabilization term (see [24]):

$$s_h^{\mathrm{BH,n}}\big((p_h, \boldsymbol{\lambda}_{\mathcal{H}}), (q_h, \boldsymbol{\xi}_{\mathcal{H}})\big) \overset{\text{def}}{=} \frac{h}{\gamma_\lambda \mu} \big(\boldsymbol{\lambda}_{\mathcal{H}} \circ \boldsymbol{\psi}_{\mathcal{H}}^{-1,n} + \llbracket p_h \rrbracket \boldsymbol{n}_\Sigma, \boldsymbol{\xi}_{\mathcal{H}} \circ \boldsymbol{\psi}_{\mathcal{H}}^{-1,n} + \llbracket q_h \rrbracket \boldsymbol{n}_\Sigma \big)_{\Sigma^n}, \tag{13}$$

where $\gamma_\lambda > 0$ is a user-defined dimensionless parameter and $\boldsymbol{\psi}_{\mathcal{H}}^n$, defined in (16), represents the discrete counterpart of the deformation map $\boldsymbol{\psi}$.

3.2. Discrete solid problem

Various discrete spaces $\boldsymbol{W}_{\mathcal{H}}$ are considered for approximating the admissible displacement space $\boldsymbol{W}$, depending on whether the 2D-shell model (4) or the 3D-shell model (2) is used.

Specifically, for the 2D-shell model (4), $\boldsymbol{W}_{\mathcal{H}} \subset \boldsymbol{W}$ is defined as the space of shell elements over the triangulation $\mathcal{T}_{\mathcal{H}}^{\Sigma}$ using linear Mixed Interpolation of Tensorial Components (MITC3) approach (see, e.g., [44, 45]). In contrast, for the 3D-shell model (2), $\boldsymbol{W}_{\mathcal{H}} \subset \boldsymbol{W}$ consists of $\mathbb{Q}_1 - \mathbb{P}_2$ tensor elements (see Figure 5). The choice of second-order approximation in the orthogonal direction to the mid-surface ensures asymptotic compatibility with the fully 3D model, while the first-order approximation enhances computational efficiency. Additionally, in both models, a reinterpolation procedure of Green-Lagrange strain components is used to mitigate numerical locking phenomena, especially for small thickness values.

Hereafter, the form $a_{\mathcal{H}}^{\mathrm{s}} : \boldsymbol{W}_{\mathcal{H}} \times \boldsymbol{W}_{\mathcal{H}} \to \mathbb{R}$ acts as a locking-free displacement-based approximation of the variational form $a^{\mathrm{s}}(\boldsymbol{d}; \boldsymbol{w})$.

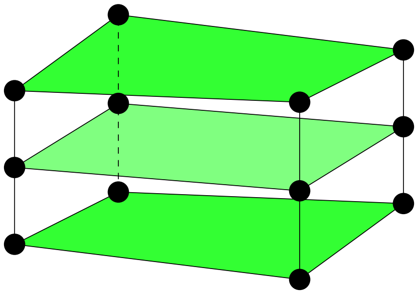

Figure 5: Example of $\mathbb{Q}_1 - \mathbb{P}_2$ tensor element.

3.2.1. Contact approximation

Following the ideas introduced in [50] for stabilization operators based on distance computation, we propose to discretize the weak form $a_{\text{contact}}(\boldsymbol{d};\boldsymbol{w})$ with a semi-implicit approach. As we have chosen a mid-point based discretization for the solid, an energy balanced discretization would be given by a midpoint discretization of a_{contact}, namely

$$a^{n+\frac{1}{2}}_{\text{contact}}(\boldsymbol{d};\boldsymbol{w}) = \int_{\Sigma^{n+\frac{1}{2}}} \kappa_{\text{c}} \Big|\text{dist}(\boldsymbol{x},\Sigma^{n+\frac{1}{2}})\Big|_{-} \boldsymbol{n}_{\Sigma^{n+\frac{1}{2}}}(\pi_{\Sigma^{n+\frac{1}{2}}}(\boldsymbol{x})) \cdot (\boldsymbol{w}(\boldsymbol{x}) - \boldsymbol{w}(\pi_{\Sigma^{n+\frac{1}{2}}}(\boldsymbol{x}))) \tag{14}$$

However, using this discretization in our formulation implies to differentiate (14) with respect to the displacement. This leads to the computation of the derivative of $\boldsymbol{n}_{\Sigma^{n+\frac{1}{2}}}(\pi_{\Sigma^{n+\frac{1}{2}}}(\boldsymbol{x}))$, hence introducing the curvature of $\Sigma^{n+\frac{1}{2}}$. We overcome this difficulty by proposing a semi-implicit version of (14) based on linearization arguments. Namely we introduce the following operator

$$\begin{aligned}
a^{n+\frac{1}{2}\sharp}_{\text{contact}}(\boldsymbol{d};\boldsymbol{w}) &= \int_{\Sigma^{n+\frac{1}{2}\sharp}} \kappa_{\text{c}} \Big|\text{dist}(\boldsymbol{x},\Sigma^{n+\frac{1}{2}\sharp})\Big|_{-} \boldsymbol{n}_{\Sigma^{n+\frac{1}{2}\sharp}}(\pi_{\Sigma^{n+\frac{1}{2}\sharp}}(\boldsymbol{x})) \cdot (\boldsymbol{w}(\boldsymbol{x}) - \boldsymbol{w}(\pi_{\Sigma^{n+\frac{1}{2}\sharp}}(\boldsymbol{x}))) \\
&+ \int_{\Sigma^{n+\frac{1}{2}\sharp}} \kappa_{\text{c}} H\left(-\text{dist}(\boldsymbol{x},\Sigma^{n+\frac{1}{2}\sharp})\right) \boldsymbol{n}_{\Sigma^{n+\frac{1}{2}\sharp}}(\pi_{\Sigma^{n+\frac{1}{2}\sharp}}(\boldsymbol{x})) \cdot \left(\boldsymbol{w}(\boldsymbol{x}) - \boldsymbol{w}(\pi_{\Sigma^{n+\frac{1}{2}\sharp}}(\boldsymbol{x}))\right) \\
&\qquad \times \boldsymbol{n}_{\Sigma^{n+\frac{1}{2}\sharp}}(\pi_{\Sigma^{n+\frac{1}{2}\sharp}}(\boldsymbol{x})) \cdot \left[\left(\boldsymbol{d}^{n+\frac{1}{2}}(\boldsymbol{x}) - \boldsymbol{d}^{n+\frac{1}{2}\sharp}(\boldsymbol{x})\right) - \left(\boldsymbol{d}^{n+\frac{1}{2}}(\pi_{\Sigma^{n+\frac{1}{2}\sharp}}(\boldsymbol{x})) - \boldsymbol{d}^{n+\frac{1}{2}\sharp}(\pi_{\Sigma^{n+\frac{1}{2}\sharp}}(\boldsymbol{x}))\right)\right],
\end{aligned} \tag{15}$$

with H the Heaviside function and $\Sigma^{n+\frac{1}{2}\sharp}$ the surface associated with $\boldsymbol{d}^{n+\frac{1}{2}\sharp}$ an extrapolation of the displacement at time $t^{n+\frac{1}{2}}$ as for instance

$$\boldsymbol{d}^{n+\frac{1}{2}\sharp} \overset{\text{def}}{=} \boldsymbol{d}^{n} + \frac{\tau}{2}\boldsymbol{u}^{\text{s},n} = \frac{3}{2}\boldsymbol{d}^{n} - \frac{1}{2}\boldsymbol{d}^{n-1}.$$

The consistency of this time scheme is justified by the following computation. As already obtained in [50] in a similar context, we have

$$\begin{aligned}
a^{n+\frac{1}{2}}_{\text{contact}}(\boldsymbol{d};\boldsymbol{w}) - a^{n+\frac{1}{2}\sharp}_{\text{contact}}(\boldsymbol{d};\boldsymbol{w}) &= -\frac{\kappa_{\text{c}}}{2} \int_{\Sigma^{n+\frac{1}{2}\sharp}} \Big|\text{dist}(\boldsymbol{x},\Sigma^{n+\frac{1}{2}\sharp})\Big|_{-} \text{D}\boldsymbol{n}_{\Sigma^{n+\frac{1}{2}\sharp}}(\pi_{\Sigma^{n+\frac{1}{2}\sharp}}(\boldsymbol{x})) \\
&\cdot \left[\left(\boldsymbol{d}^{n+\frac{1}{2}}(\boldsymbol{x}) - \boldsymbol{d}^{n+\frac{1}{2}\sharp}(\boldsymbol{x})\right) - \left(\boldsymbol{d}^{n+\frac{1}{2}}(\pi_{\Sigma^{n+\frac{1}{2}\sharp}}(\boldsymbol{x})) - \boldsymbol{d}^{n+\frac{1}{2}\sharp}(\pi_{\Sigma^{n+\frac{1}{2}\sharp}}(\boldsymbol{x}))\right)\right] + O\left(\frac{\kappa_{\text{c}}}{2}\left\|\boldsymbol{d}^{n+\frac{1}{2}} - \boldsymbol{d}^{n+\frac{1}{2}\sharp}\right\|^2\right).
\end{aligned}$$

We have seen that $\kappa_{\text{c}}\Big|\text{dist}(\boldsymbol{x},\Sigma^{n+\frac{1}{2}\sharp})\Big|_{-}$ is the contact force per surface unit, hence it remains finite. This leads to the relation

$$a^{n+\frac{1}{2}}_{\text{contact}}(\boldsymbol{d};\boldsymbol{w}) - a^{n+\frac{1}{2}\sharp}_{\text{contact}}(\boldsymbol{d};\boldsymbol{w}) = O\Big(\frac{\kappa_{\text{c}}}{2}\left\|\boldsymbol{d}^{n+\frac{1}{2}} - \boldsymbol{d}^{n+\frac{1}{2}\sharp}\right\|\Big) O\Big(1 + \kappa_{\text{c}}\left\|\boldsymbol{d}^{n+\frac{1}{2}} - \boldsymbol{d}^{n+\frac{1}{2}\sharp}\right\|^2\Big).$$

Therefore, with the above choice of extrapolation, we get

$$a^{n+\frac{1}{2}}_{\text{contact}}(\boldsymbol{d};\boldsymbol{w}) - a^{n+\frac{1}{2}\sharp}_{\text{contact}}(\boldsymbol{d};\boldsymbol{w}) = O\big(\tau^2 + \kappa_{\text{c}}\tau^4\big).$$

As a consequence, there exists for any large value of κ_{c} a sufficiently small time step such that our semi-implicit time scheme based on a linearization procedure does not alter the order two consistency of our midpoint time scheme.

3.3. Coupling scheme

In order to mitigate the computation complexity of the discrete problem, the geometric coupling $(3)_1$ is treated in a explicit fashion, so that we set

$$\boldsymbol{\psi}^n = \boldsymbol{I}_\Sigma + \boldsymbol{d}^{n-1} \text{ on } \Sigma, \quad \Sigma^n = \boldsymbol{\psi}^n(\Sigma).$$

Meanwhile, coupling conditions $(3)_{2,3}$ are enforced implicitly, resulting in a semi-implicit strongly coupled scheme. The proposed discrete approximation of (8) is detailed in Algorithm 1.

Algorithm 1: Fictitious domain strongly coupled scheme.

For $n \geq 1$:

1. Interface update:

$$\boldsymbol{\psi}^n_{\mathcal{H}} = \boldsymbol{I}_\Sigma + \boldsymbol{d}^{n-1}_{\mathcal{H}} \text{ on } \Sigma, \qquad \Sigma^n = \boldsymbol{\psi}^n_{\mathcal{H}}(\Sigma). \tag{16}$$

2. Find $\big(\boldsymbol{u}^n_h, p^n_h, \lambda^n_{\mathcal{H}}, \boldsymbol{d}^n_{\mathcal{H}}\big) \in \boldsymbol{V}_h \times Q^n_h \times \boldsymbol{\Lambda}_{\mathcal{H}} \times \boldsymbol{W}_{\mathcal{H}}$, with $\boldsymbol{u}^{\text{s},n-\frac{1}{2}}_{\mathcal{H}} = \partial_\tau \boldsymbol{d}^n_{\mathcal{H}}$, such that

$$\begin{aligned}\rho^{\text{f}}\left(\partial_\tau \boldsymbol{u}^n_h, \boldsymbol{v}_h\right)_{\Omega^{\text{f}}} + a^{\text{f}}_h\big(\boldsymbol{u}^{n-1}_h; (\boldsymbol{u}^n_h, p^n_h), (\boldsymbol{v}_h, q_h)\big) + \rho^{\text{s}}\big(\partial_\tau \boldsymbol{u}^{\text{s},n}_{\mathcal{H}}, \xi_{\mathcal{H}}\big)_{\text{s}} + a^{\text{s}}_{\mathcal{H}}\big(\boldsymbol{d}^{n-\frac{1}{2}}_{\mathcal{H}}; \xi_{\mathcal{H}}\big)\\ - b\big(\lambda^n_{\mathcal{H}}, \boldsymbol{v}_h \circ \boldsymbol{\psi}^n_{\mathcal{H}} - \boldsymbol{w}_{\mathcal{H}}\big) + b\big(\xi_{\mathcal{H}}, \boldsymbol{u}^n_h \circ \boldsymbol{\psi}^n_{\mathcal{H}} - \boldsymbol{u}^{\text{s},n-\frac{1}{2}}_{\mathcal{H}}\big) + s^{\text{BH,n}}_h\big((p^n_h, \lambda^n_{\mathcal{H}}), (q_h, \xi_{\mathcal{H}})\big) = 0\end{aligned} \tag{17}$$

for all $\big(\boldsymbol{v}_h, q_h, \xi_{\mathcal{H}}, \boldsymbol{w}_{\mathcal{H}}\big) \in \boldsymbol{V}_h \times Q^n_h \times \boldsymbol{\Lambda}_{\mathcal{H}} \times \boldsymbol{W}_{\mathcal{H}}$.

---

4. Numerical examples

The present section aims to provide a comprehensive numerical investigation to illustrate the capability of the methods proposed in Algorithm 1 in various scenarios. It is divided into three parts, each focusing on different aspects. Section 4.1 is dedicated to illustrating the accuracy of Algorithm 1 with respect to well-established methods documented in the existing literature. To this purpose, we consider a series of 2D immersed FSI benchmarks. In Section 4.1.2, we compare the approximations provided by Algorithm 1 in both the case of the 2D-shell and 3D-shell models. Finally, Section 4.3 presents the application of Algorithm 1 to the simulation of the dynamics of the aortic valve, where we in particular highlight the benefits of the additional mass constraint. In all subsequent sections, the strongly coupled problem (17) in Algorithm 1 is solved using a partitioned solution procedure. This procedure is parameter-free and relies on interface Newton-GMRES Dirichlet–Neumann iterations (see, e.g., [28, 26]). Throughout the following sections, all physical quantities and parameters are expressed in the centimeter-gram-second (CGS) unit system.

4.1. Comparative study

In this section, we present a comprehensive numerical study in order to assess the accuracy of the method introduced in Algorithm 1 (referred to as FD-LJ hereafter), with respect to alternative unfitted mesh methods (see, e.g., [14] for a review). These include the Nitsche-XFEM method (denoted as NXFEM), the standard penalty fictitious domain method (FD), and a modified version of the latter incorporating enhanced interfacial mass conservation through the "grav-div" stabilization technique (FD-GD). The Arbitrary Lagrangian-Eulerian method (denoted by ALE) with high-resolution space-time grids is considered as reference for the comparisons.

The accuracy of the unfitted mesh methods is assessed using three successive space-time refinement levels: *M1*, *M2*, and *M3*. These levels correspond to uniform refinements of *M1*, with refinement factors of 2 and 4 in both spatial and temporal directions. Specifically, the spatial grids consist of uniform structured meshes, as illustrated in Figure 6. Detailed descriptions of these refinement levels are provided subsequently for each benchmark. In all tests, the structure is described by a nonlinear Timoshenko curved beam model with MITC spatial discretization (see, e.g., [55, 48]).

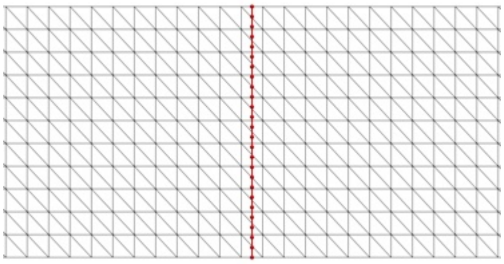

Figure 6: Illustration of the structured meshes used in the benchmark of Section 4.1. The fluid mesh is represented in gray, while the structure mesh is highlighted in red.

In the following, we present three distinct 2D benchmark problems that cover a wide range of scenarios, motivated by bio-fluid flow simulations, including partially and fully intersected fluid domains. For the NXFEM method, the following parameters remain constant across all test cases: $\gamma_\mathrm{v} = \gamma_\mathrm{p} = 0.01$, $\gamma_\mathrm{g} = 1$, and $\gamma = 100$. For all other methods, we set $\gamma_\mathrm{p} = 1$ and $\gamma_\mathrm{d} = 0$, except for FD-GD, where $\gamma_\mathrm{d} = 1$. Additional parameter details are provided subsequently for each benchmark.

All the numerical simulations of the present section have been performed with the `FELiScE` finite element library[1].

4.1.1. Idealized closed valve

As a first example, we consider a benchmark problem mimicking the behavior of a closed valve subjected to a pressure drop (see, e.g., [41, 66]). The problem consists in an elastic beam clamped at its endpoints on Γ_bot and Γ_top and immersed in a channel filled with an incompressible Newtonian fluid, as represented in Figure 7. The fluid domain's geometry (see Figure 7) is defined by $\Omega = (0, 4) \times (0, 1)$, while the reference solid configuration is given by $\Sigma = \{2\} \times (0, 1)$. The time domain spans $t \in [0, 3]$, representing the duration required for the system to reach a steady state from its initial rest state. Regarding the fluid's boundary conditions, no-slip boundary conditions are enforced on Γ_bot and Γ_top, whereas zero traction is enforced on the lateral boundary Γ_out. On the inlet boundary Γ_in, a time-dependent traction force is applied as $\boldsymbol{\sigma}^\mathrm{f}(\boldsymbol{u}, p) = -p_\mathrm{in}\boldsymbol{n}$, with the inlet pressure given by

$$p_{in}(t) = 3 \cdot 10^5 \ \mathrm{atanh}(10\, t).$$

The physical parameters of the fluid are set to $\rho^\mathrm{f} = 100$ and $\mu = 10$, while for the solid the parameters we take the values $\rho^\mathrm{s} = 100$, $\epsilon = 0.0212$, $E = 5.6 \cdot 10^7$, and $\nu = 0.4$.

Spatial and temporal discretization. Table 1 provides details regarding the space-time grid used for the ALE method, as well as the three refinement levels (*M1*, *M2*, and *M3*) employed for the unfitted mesh methods. Additionally, across all refinement levels, the parameters ϵ and γ_gd for the FD and FD-GD methods are set to 10^{-5} and 10^{-4}, respectively. For a detailed and comprehensive discussion about the value of the parameter γ_gd, we refer to [14, Section 4.2.3]. The parameter γ_λ for the FD-LJ is set to 10 for all the refinement levels. Additionally, since the interface Σ^n divides the domain Ω into two subdomains, Ω_1^n and Ω_2^n, at each time step (see, e.g., Figure 7 for $n = 0$), there is no necessity to introduce the fictitious interface Σ_fic for the definition of the pressure space Q_h^n in (9).

Comparison of the results. Once the prescribed pressure is established, the elastic solid initiates its deformation, leading to bending and elongation. After a brief initial transition phase, the system gradually reaches a steady state

---

[1] `https://gitlab.inria.fr/felisce/felisce`

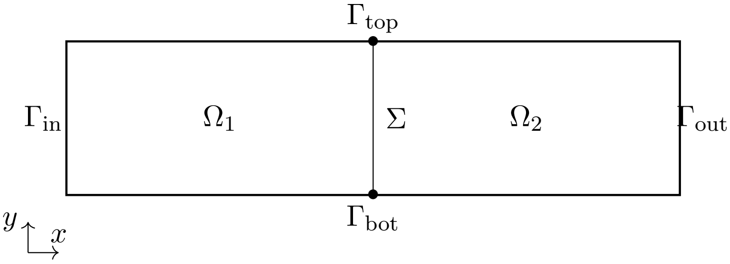

Figure 7: Idealized closed valve geometric configuration.

	Number of elements		Time step
	Fluid mesh	**Structure mesh**	
ALE	25600	80	$2.5 \cdot 10^{-4}$
M1	1034	24	$2 \cdot 10^{-3}$
M2	4370	50	$1 \cdot 10^{-3}$
M3	17954	100	$5 \cdot 10^{-4}$

Table 1
Idealized closed valve space-time grids details.

characterized by a constant pressure jump across the interface. In this state, both fluid and solid velocities become negligible, and the pressure becomes a piecewise constant function. Specifically, it takes the values of $3{\times}10^5$ on one side of the interface and zero on the other side. For comparison purposes, we consider the results at $t = 0.125$. In particular

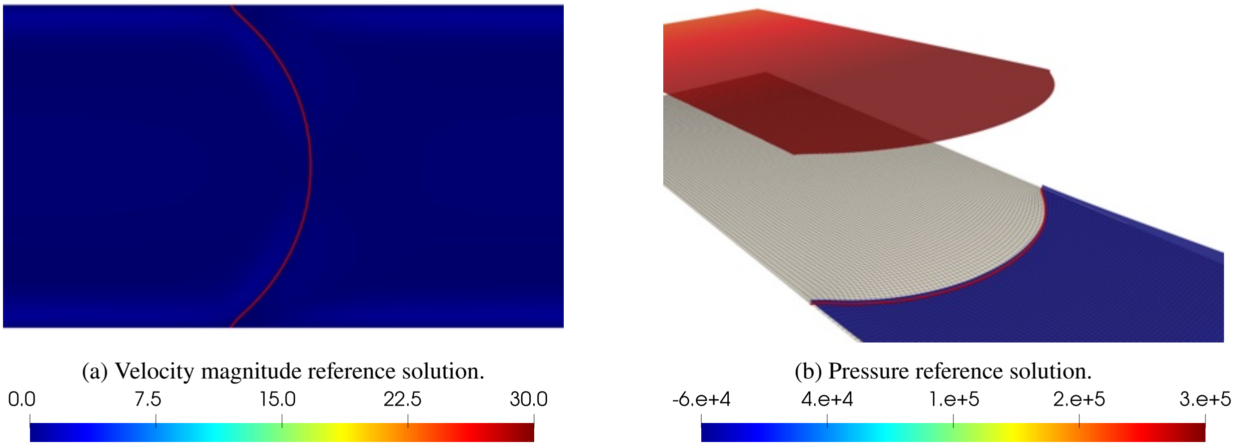

(a) Velocity magnitude reference solution.

(b) Pressure reference solution.

Figure 8: Snapshots of the velocity magnitude and pressure at $t = 0.125$ for the reference solution.

Figure 8b shows the reference solution obtained using the fitted mesh ALE method, while Figures 9–14 depict the results obtained with the four unfitted mesh methods in term of velocity magnitude and pressure for the three refinement levels. From these results, it is evident that regardless of the refinement level employed, the FD method exhibits a spurious flow within the channel (see Figures 9b, 10b, 11b) and consequently yields a significantly underestimated pressure in comparison to the reference solution, see Figures 8b, 12b, 13b, 14b. This is a well-known limitation of the FD method with continuous pressure approximations (see, e.g., [4, 41]). Although global mass conservation in the whole domain Ω is ensured, the continuous nature of the pressure approximation fails to guarantee local mass conservation on each side of the interface. This limitation is effectively fixed by the other unfitted mesh methods under consideration. The FD-LJ method overcomes this issue via the enriched finite element pressure space, thus significantly

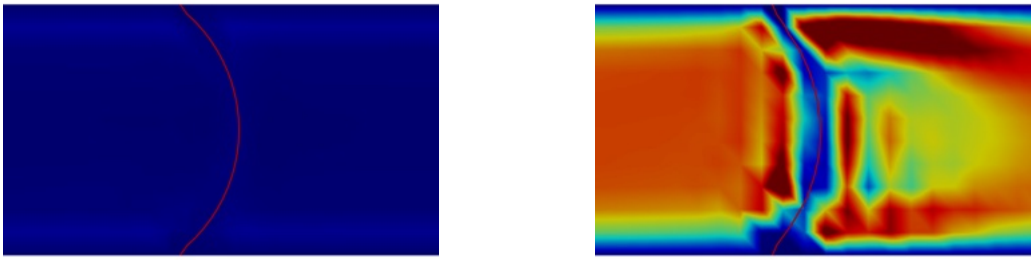

(a) NXFEM method. (b) FD method.

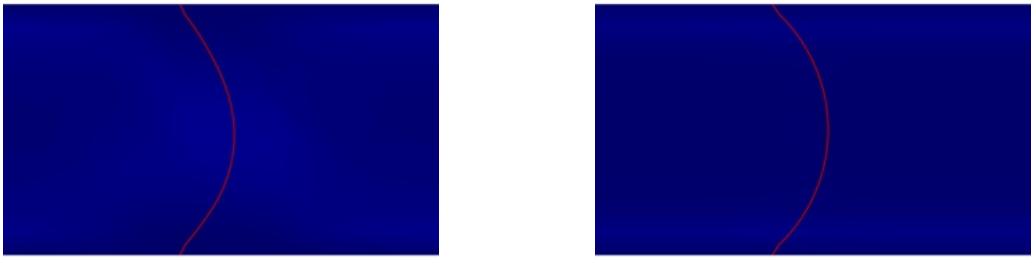

(c) FD-GD method. (d) FD-LJ method.

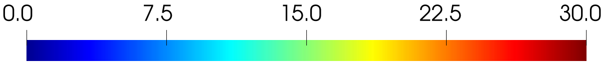

Figure 9: Snapshots of the fluid velocity magnitude at $t = 0.125$ for the *M1* refinement level.

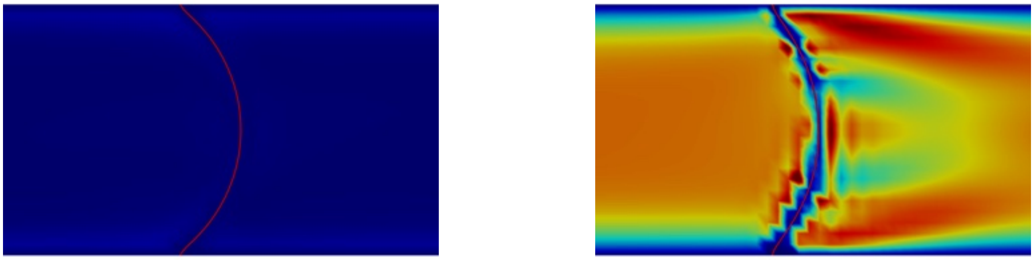

(a) NXFEM method. (b) FD method.

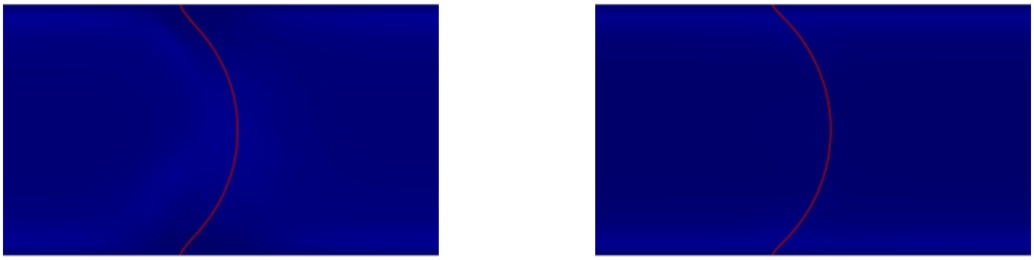

(c) FD-GD method. (d) FD-LJ method

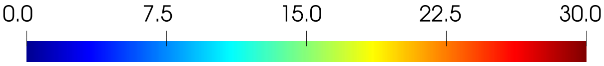

Figure 10: Snapshots of the fluid velocity magnitude at $t = 0.125$ for the *M2* refinement level.

improving the mass conservation constraint within each subdomain. The additional basis function in the pressure space facilitates the retrieval of the correct pressure discontinuity across the interface (see Figures 12d, 13d, 14d) and the

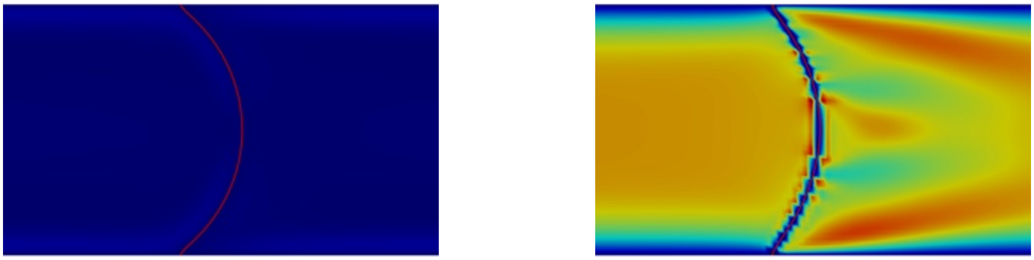

(a) NXFEM method.

(b) FD method.

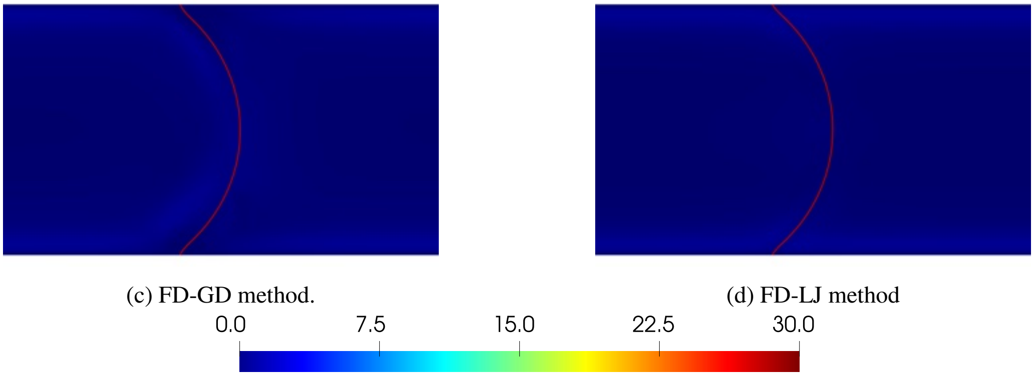

(c) FD-GD method.

(d) FD-LJ method

Figure 11: Snapshots of the fluid velocity magnitude at $t = 0.125$ for the *M3* refinement level.

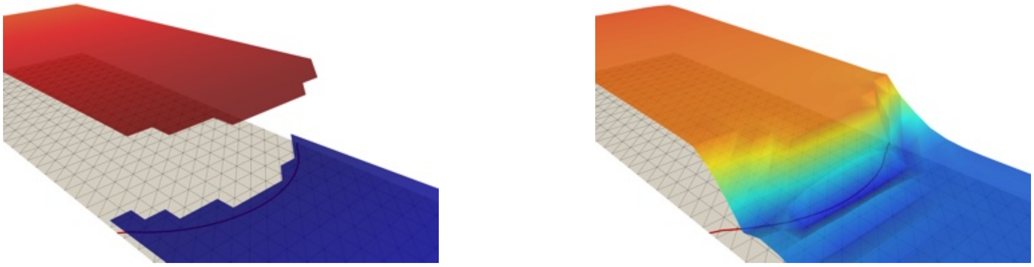

(a) NXFEM method.

(b) FD method.

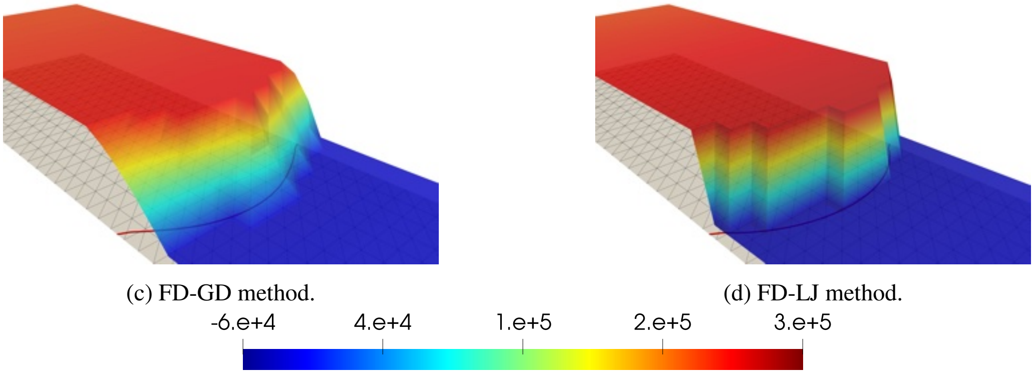

(c) FD-GD method.

(d) FD-LJ method.

Figure 12: Snapshots of the fluid pressure at $t = 0.125$ for the *M1* refinement level.

correct velocity field (see Figures 9d, 10d, 11d). On the other hand, the NXFEM method correctly retrieves the velocity and pressure jump via the use of overlapping finite element spaces for the velocity and the pressure, thereby allowing

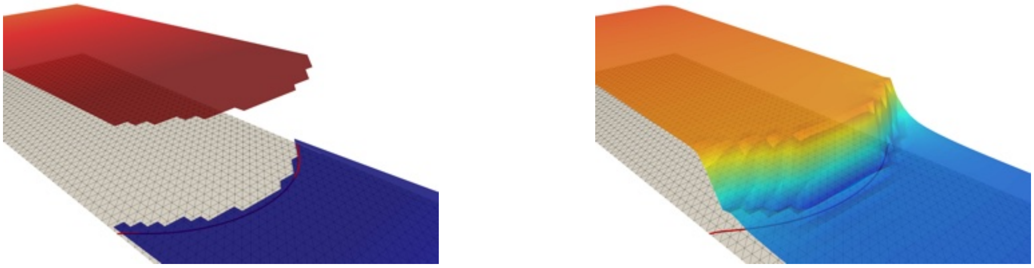

(a) NXFEM method.

(b) FD method.

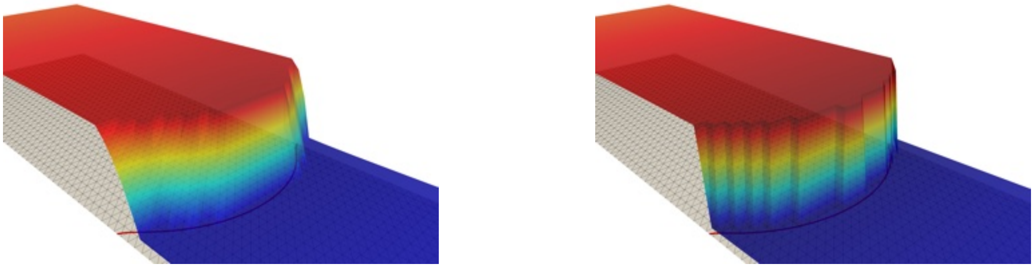

(c) FD-GD method.

(d) FD-LJ method.

Figure 13: Snapshots of the fluid pressure at $t = 0.125$ for the *M2* refinement level.

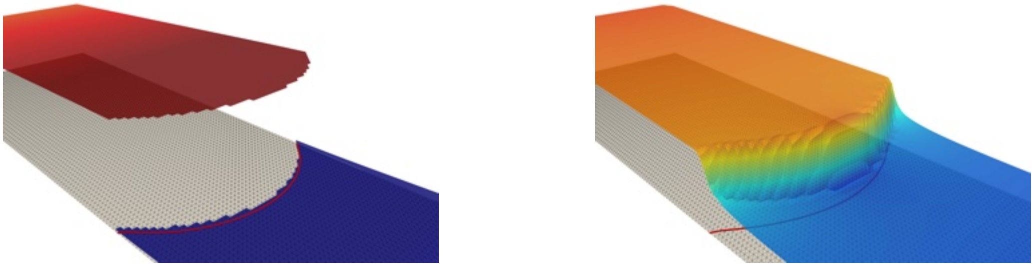

(a) NXFEM method.

(b) FD method.

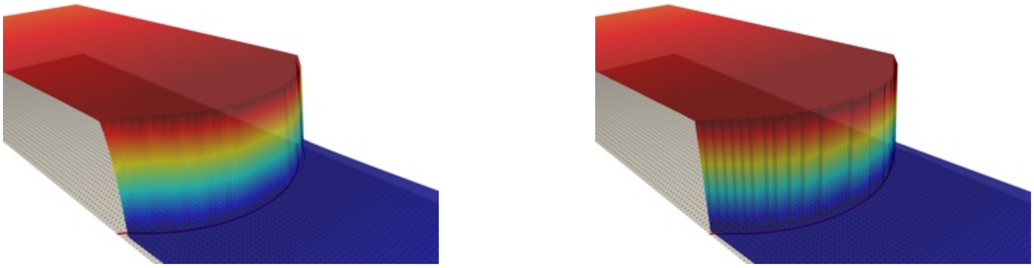

(c) FD-GD method.

(d) FD-LJ method.

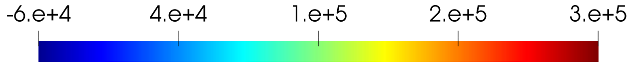

Figure 14: Snapshots of the fluid pressure at $t = 0.125$ for the *M3* refinement level.

weak and strong discontinuities across the interface. The results are illustrated in Figures 9a, 10a, 11a and Figures 12a, 13a, 14a for velocity and pressure, respectively. Furthermore, the comparisons also show that as expected the FD-GD method removes the spurious velocity field of the FD method. Indeed, the grad-div penalty term enhances the local satisfaction of the mass conservation constraint in the vicinity of the interface (see, e.g., [41]), and thus significantly reduces the mass leak across the interface, as shown in Figures 9c, 10c, 11c. Although not exhibiting a discontinuous pressure across the interface, it demonstrates excellent agreement compared to the reference solution, as depicted in Figures 12c, 13c, 14c.

Figure 15 provides a temporal comparison of the horizontal displacement at the mid-point of the interface. The FD-LJ, NXFEM, and FD-GD methods exhibit better agreement, increasing with mesh refinement, with the reference solution compared to the FD method. In particular, unlike the other methods, the FD method fails to capture the dynamics of the structure.

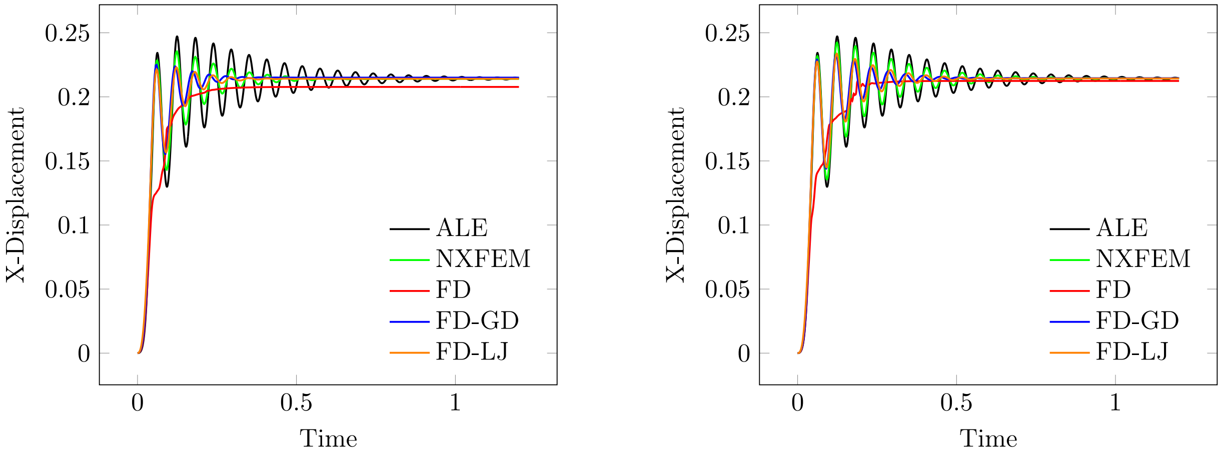

(a) *M1* vs. Reference.

(b) *M2* vs. Reference.

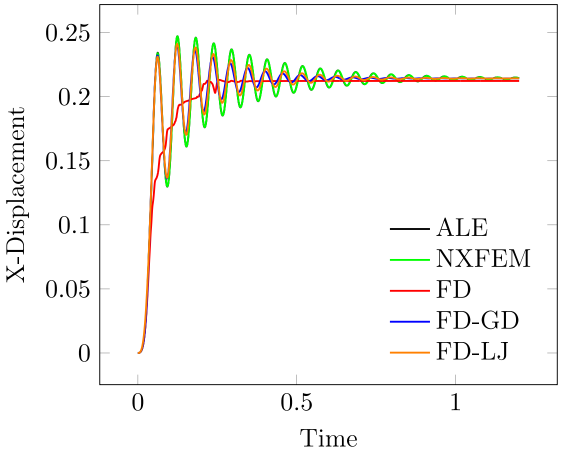

(c) *M3* vs. Reference.

Figure 15: Time history of the x-displacement of the solid mid-point.

4.1.2. Idealized open valve

As a second example, we consider the benchmark problem proposed in several studies [32, 38, 41, 70], focusing on simulating the behavior of a section of an idealized heart valve. The 2D representation of the heart valve comprises two identical cantilevered elastic beams attached to the walls of a 2D channel filled with an incompressible Newtonian fluid. Figure 16 shows the initial geometric configuration. Due to the symmetry of the problem, simulations are performed on half of the domain, incorporating appropriate symmetry boundary conditions. The fluid domain is defined as $\Omega = (0, 8) \times (0, 0.805)$, while the reference configuration of the solid is $\Sigma = \{2\} \times (0, 0.7)$. The simulation spans a time interval of $[0, 3]$, roughly corresponding to three full cycles of oscillations of the structure. The following conditions

	Number of elements		**Time step**
	Fluid mesh	**Structure mesh**	
ALE	48706	59	$1 \cdot 10^{-3}$
M1	4096	25	$1 \cdot 10^{-2}$
M2	20352	64	$5 \cdot 10^{-3}$
M3	65536	128	$2.5 \cdot 10^{-3}$

Table 2
Idealized open valve space-time grids details.

are applied on the fluid domain boundaries: a no-slip condition on Γ_{bot}, a symmetry condition on Γ_{top}, and zero traction on the lateral boundary Γ_{out}. Additionally, a prescribed velocity profile is enforced on boundary Γ_{in}, given by:

$$\boldsymbol{u}(t) = -5y(1.61 - y)\,\mathrm{atanh}(5t)(\sin(2\pi t) + 1.1)\boldsymbol{n}.$$

The beam is fully clamped at its bottom endpoint. Both the fluid and the solid are initially at rest. The physical parameters for this example are as follows: fluid density $\rho^{\text{f}} = 100$, fluid viscosity $\mu = 10$, solid density $\rho^{\text{s}} = 100$, and the remaining solid parameters are $\epsilon = 0.0212$, $E = 5.6 \cdot 10^{7}$, and $\nu = 0.4$.

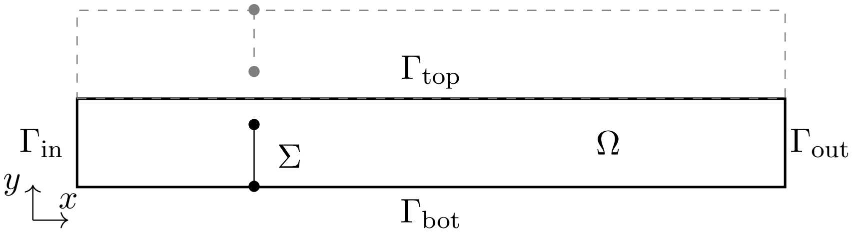

Figure 16: Idealized open valve geometric configuration.

Spatial and temporal discretization. Table 2 presents details of the space-time grid used in the ALE method, as well as the configurations for three refinement levels: *M1*, *M2*, and *M3*. In the ALE method, the fluid mesh is refined around the coupling interface. Due to the significant deflection experienced by the interface, the mesh motion is performed using a pseudo-nonlinear elastic extension (see [43]). Regarding the FD and FD-GD methods, the penalty parameter ε takes values of 10^{-5}, 10^{-6}, and 10^{-6} for *M1*, *M2*, and *M3*, respectively. The parameter γ_{gd} in the FD-GD method is set to 10^{-4} for all refinement levels. For the FD-LJ method, $\gamma_{\lambda} = 10$. For the FD-LJ method, to accurately define the discrete pressure space Q_h^n in (9), we employ the fictitious interface Σ_{fic}^n, obtained by projecting, at each time step, the endpoint of the structure onto the boundary Γ_{top}, as illustrated in Figure 17.

Comparison of the results. The parabolic and oscillatory velocity profile induces a deformation of the interface, causing it to flex and subsequently return to a position near its initial state, oscillating over time. For comparison purposes, we consider the time instant $t = 0.5$, corresponding to the point where the valve achieves its maximum displacement. Figure 18 illustrates the reference solution obtained using the fitted mesh ALE approach.

Overall, there is a notable agreement in both velocity and pressure fields across all methods for all refinement levels, as it can be inferred from Figures 19–24. In particular, the FD-LJ and NXFEM methods exhibit a very good agreement with the results of the ALE method from the initial refinement level *M1* (see Figures 19d, 19a, 22d, and 12a). Subsequent refinement further enhances the agreement with the reference solution for all methodologies. Starting from refinement level *M2*, the FD-GD method provides results in close agreement with the reference solution (see Figures 20c and 23c). Notably, for the FD approach, comparing results between *M1* and *M3* clearly illustrates the positive impact of mesh refinement on the accuracy (see Figures 22b–24b).

Similar observations can be drawn from Figure 25, which provides a comparison of the temporal evolution of the displacement in the x and y directions of the upper leaflet tip. Both the FD-LJ and NXFEM methods exhibit good

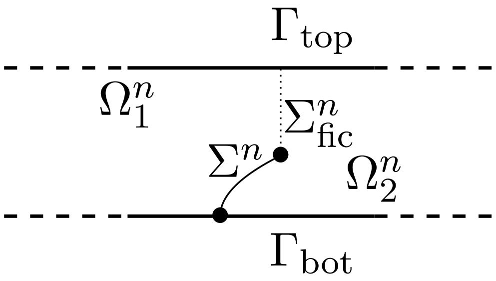

Figure 17: Example of the splitting of the fluid domain Ω into Ω_1^n and Ω_2^n using the fictitious interface Σ_{fic}^n.

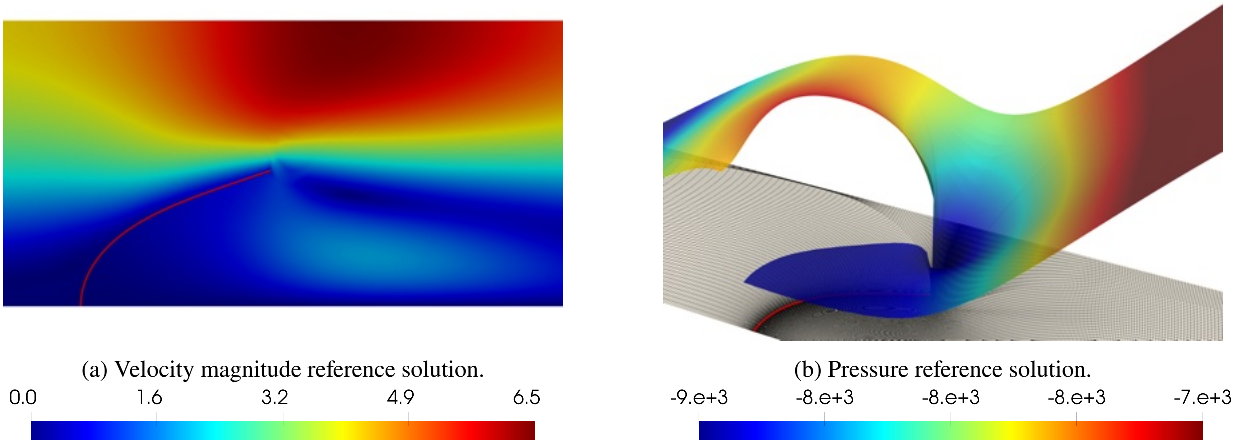
(a) Velocity magnitude reference solution.

(b) Pressure reference solution.

Figure 18: Snapshots of the velocity magnitude and pressure at $t = 0.5$ for the reference solution.

agreement with the ALE method. However, the overall agreement of the FD-GD methods is satisfactory for the *M2* and *M3* refinement levels. Additionally, as mesh refinement increases, the convergence of the FD method solutions towards the reference solution is clearly visible.

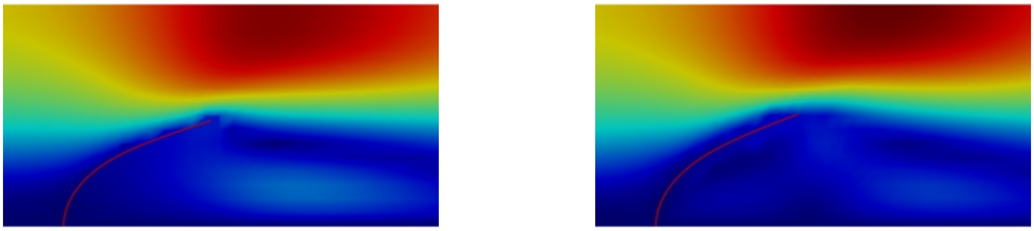

(a) NXFEM method.

(b) FD method.

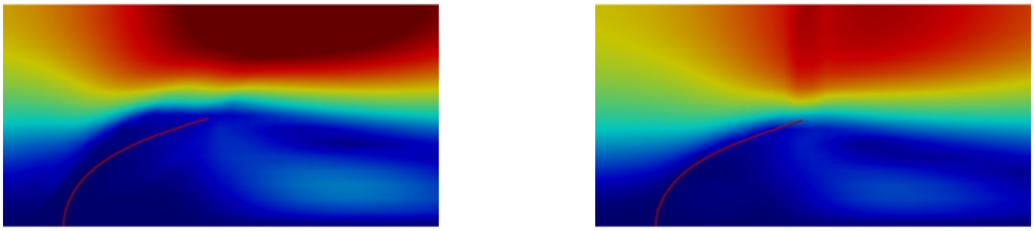

(c) FD-GD method.

(d) FD-LJ method.

Figure 19: Snapshots of the fluid velocity magnitude at $t = 0.5$ for the *M1* refinement level.

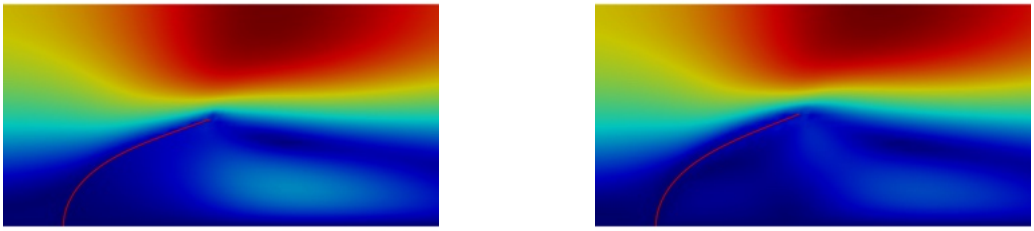

(a) NXFEM method.

(b) FD method.

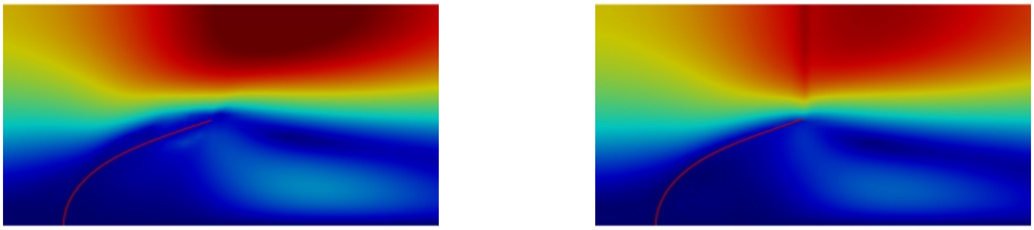

(c) FD-GD method.

(d) FD-LJ method.

Figure 20: Snapshots of the fluid velocity magnitude at $t = 0.5$ for the *M2* refinement level.

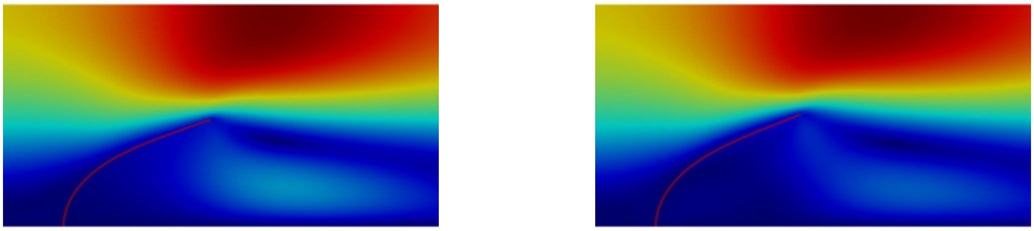

(a) NXFEM method. (b) FD method.

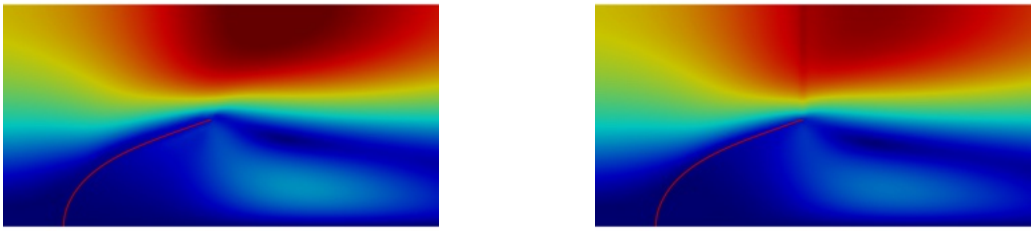

(c) FD-GD method. (d) FD-LJ method.

Figure 21: Snapshots of the fluid velocity magnitude at $t = 0.5$ for the *M3* refinement level.

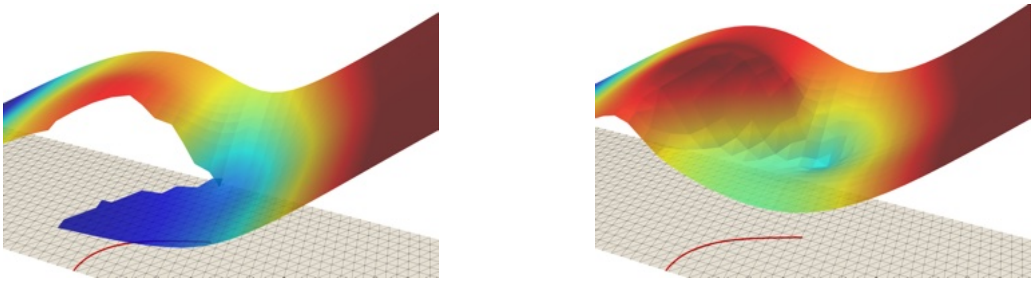

(a) NXFEM method. (b) FD method.

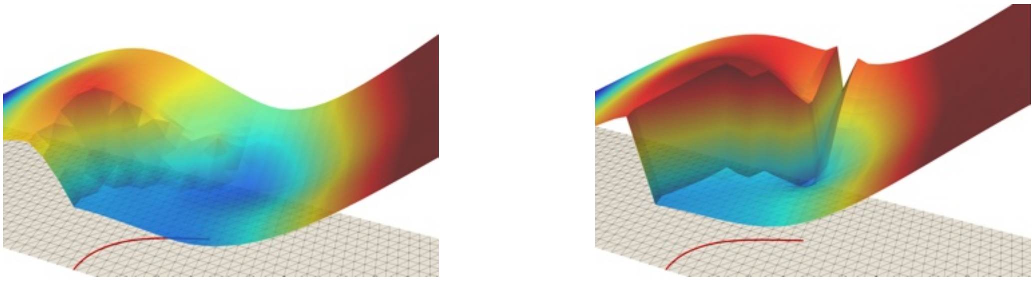

(c) FD-GD method. (d) FD-LJ method.

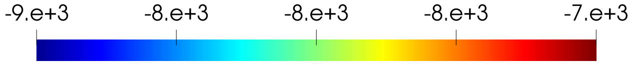

Figure 22: Snapshots of the fluid pressure at $t = 0.5$ for the *M1* refinement level.

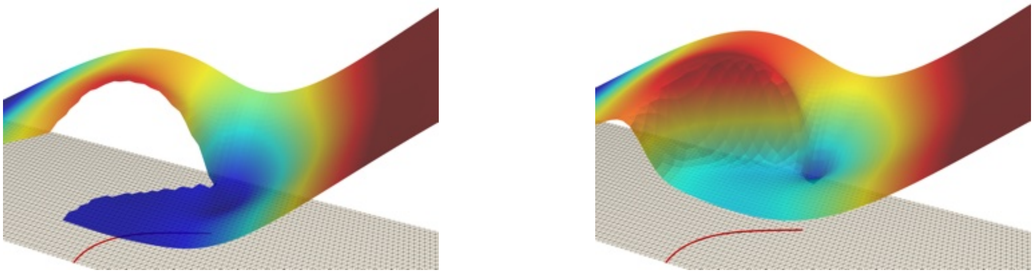

(a) NXFEM method.

(b) FD method.

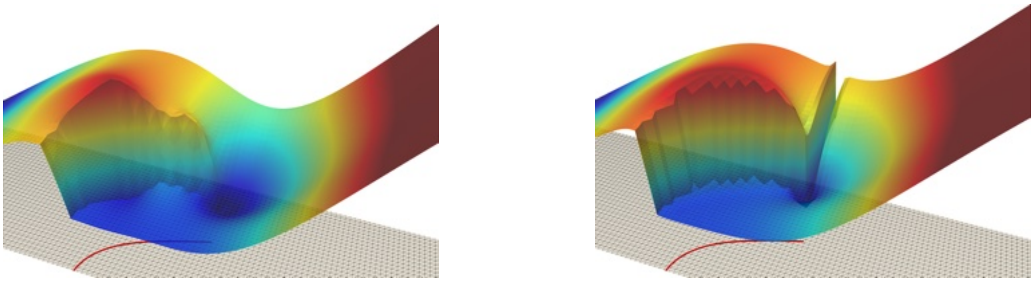

(c) FD-GD method.

(d) FD-LJ method.

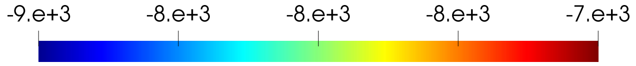

Figure 23: Snapshots of the fluid pressure at $t = 0.5$ for the *M2* refinement level.

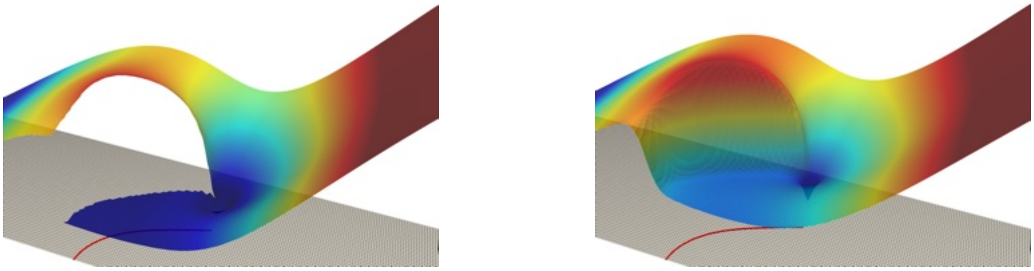

(a) NXFEM method.

(b) FD method.

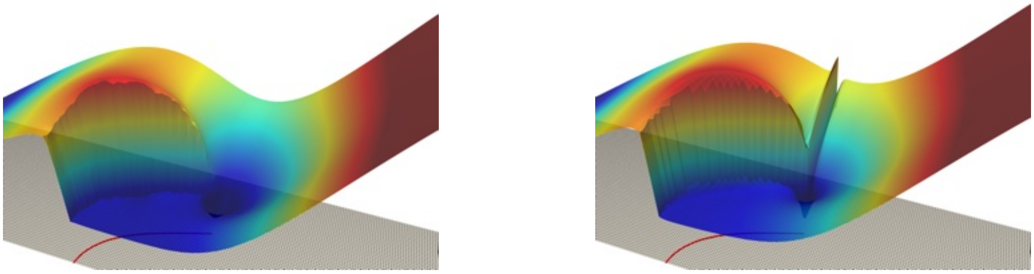

(c) FD-GD method.

(d) FD-LJ method.

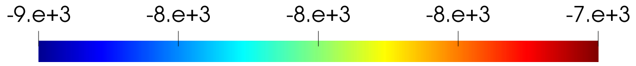

Figure 24: Snapshots of the fluid pressure at $t = 0.5$ for the *M3* refinement level.

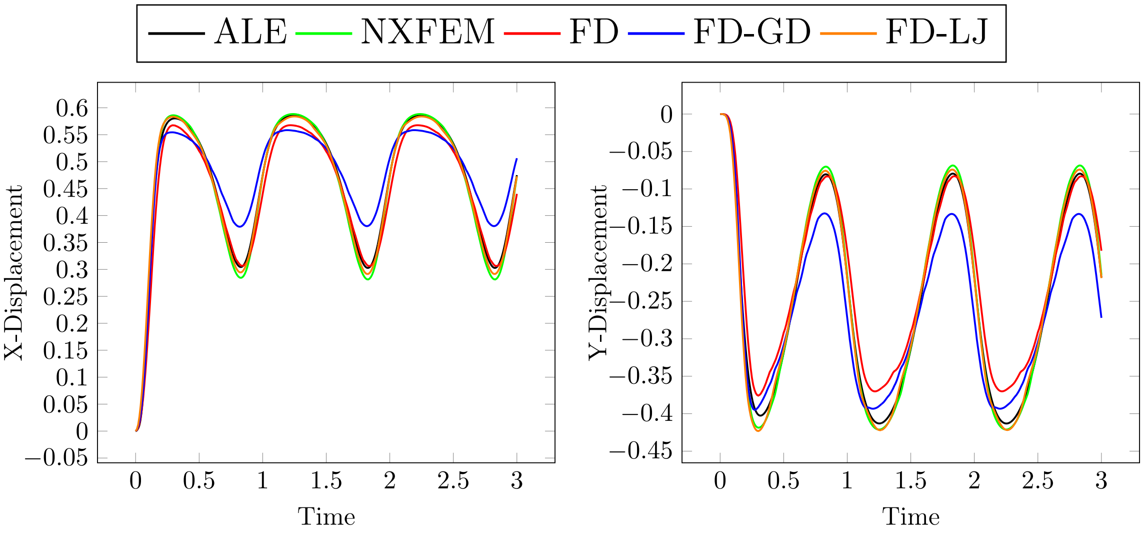

(b) *M1* vs. Reference.

(c) *M1* vs. Reference.

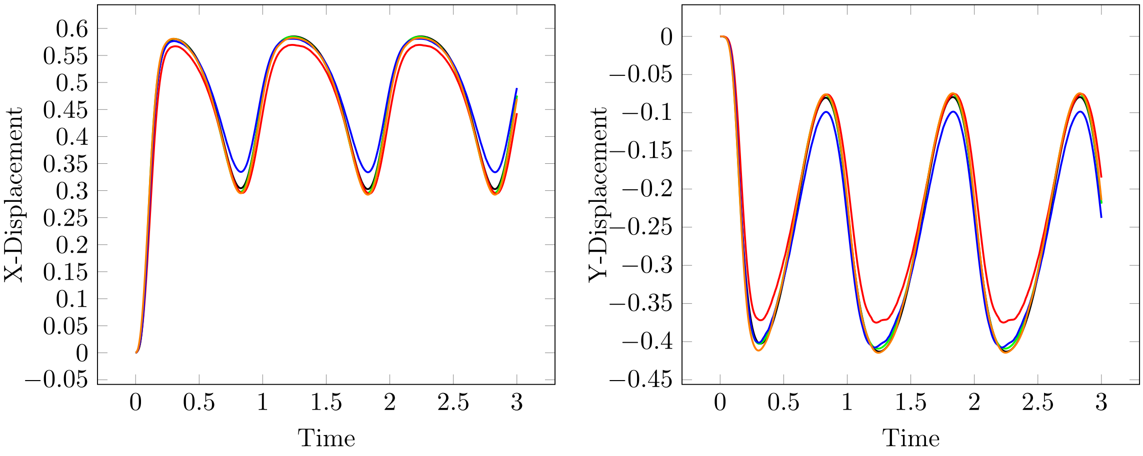

(d) *M2* vs. Reference.

(e) *M2* vs. Reference.

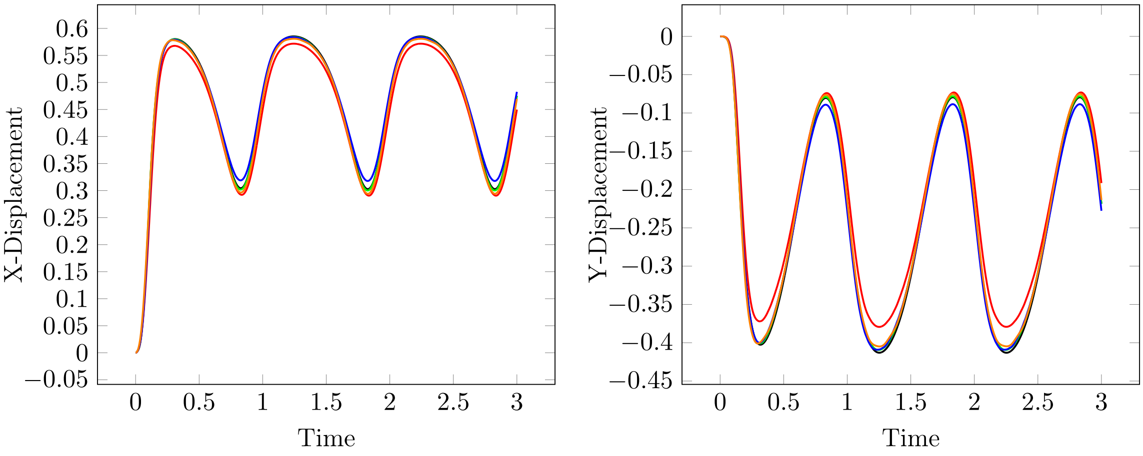

(f) *M3* vs. Reference.

(g) *M3* vs. Reference.

Figure 25: Time history of the x-displacement (left) and y-displacement (right) of the valve end-point.

4.1.3. Vesicle in a lid-driven cavity flow

As last example, we consider the lid-driven cavity benchmark problem featuring an immersed elastic vesicle, as presented in [67, 34, 57, 33]. The fluid domain is defined as the rectangular region $\Omega = (0, 1) \times (0, 1)$. The reference configuration Σ of the structure, corresponds to a circle centered at $(0.6, 0.5)$ with a radius of $R = 0.2$. Figure 26 shows the initial geometric configuration. The simulation spans a time interval of 10 seconds, representing the period required for a complete revolution of the vesicle within the fluid domain. A no-slip boundary condition is enforced on Γ_{wall}, while zero traction is applied to the lateral boundaries Γ_{in} and Γ_{out}. On the upper boundary Γ_{top}, a prescribed velocity profile of $\boldsymbol{u} = (1, 0)$ is specified. Initially, both the fluid and the solid are at rest. The physical parameters are chosen as follows: $\rho^{\mathrm{f}} = 100$, $\mu = 10$, $\rho^{\mathrm{s}} = 100$, $\epsilon = 0.0212$, $E = 5.6 \cdot 10^3$, and $\nu = 0.4$.

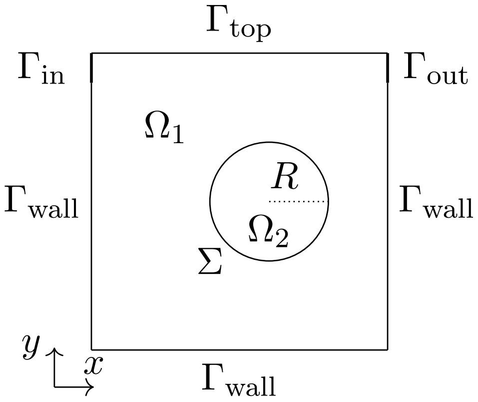

Figure 26: Lid-driven cavity geometric configuration.

Spatial and temporal discretization. Table 3 provides details of the space-time grid utilized in the fitted mesh ALE approach and the grids corresponding to refinement levels *M1*, *M2*, and *M3*. For defining the discrete pressure space Q_h for the FD-LJ method, we designate Ω_1^n as the portion of the domain Ω outside Σ^n, while the portion of the domain within Σ^n is labeled as Ω_2^n (see Figure 26). In this scenario, there is no need for the artificial interface Σ_{fic} to subdivide the domain. It is essential to note that the choice of subdomains is arbitrary; selecting the opposite subdomains yields the same result. The penalty parameter ϵ for the FD and FD-GD methods remains constant at $\epsilon = 10^{-4}$ across all refinement levels. Concerning the stabilization parameter γ_{gd}, we set $\gamma_{\mathrm{gd}} = 1$ for *M1*, $\gamma_{\mathrm{gd}} = 10^{-1}$ for *M2*, and $\gamma_{\mathrm{gd}} = 10^{-4}$ for *M3*. Additional details regarding the specific values of the stabilization parameter γ_{gd} can be found in [14, Section 4.3.3]. The parameter γ_λ for the FD-LJ method is set to 10 for all refinement levels.

Comparison of the results. We consider that $t = 4.5$ is the upper limit where we can still refer to the ALE solution as the reference (close to the break-down of the mesh motion procedure, which is performed without remeshing or mesh topology changes, see Figure 27).

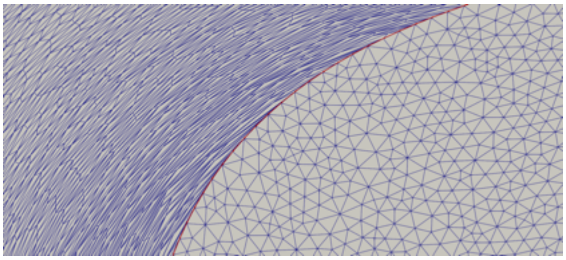

Figure 27: Close-up view of the ALE fluid mesh at time $t = 0.45$. Distortions in the elements lead to the breakdown of the mesh motion procedure.

	Number of elements		Time step
	Fluid mesh	**Structure mesh**	
ALE	46078	200	$2.5 \cdot 10^{-3}$
M1	800	40	$1 \cdot 10^{-2}$
M2	3200	80	$5 \cdot 10^{-3}$
M3	12800	160	$2.5 \cdot 10^{-3}$

Table 3
Lid-driven cavity space-time grids details.

Figures 32–34 present the snapshots of the fluid pressure at $t = 4.5$ for three refinement levels, while Figures 29–31 show the snapshots of the fluid velocity magnitude and the vesicle position at the same time instance and refinement levels.

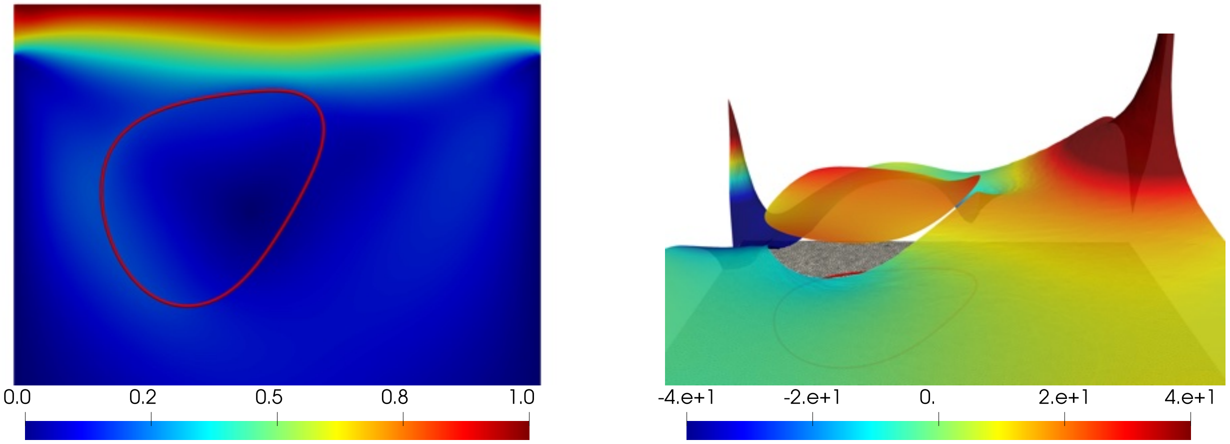

(c) Velocity magnitude reference solution.

(d) Pressure reference solution.

Figure 28: Snapshots of the velocity magnitude and pressure at $t = 4.5$ for the reference solution.

We observe that the FD-LJ and NXFEM methods accurately approximate the interface location even with the coarsest refinement levels (see Figures 29a,d–31a,d).

These methods also effectively capture the pressure jump between the inner vesicle and the cavity, with further improvement observed with mesh refinement (see Figures 32a,d–34a,d). Moreover, the FD-GD method achieves satisfactory approximation to the reference solution starting from refinement level *M2*, as depicted in Figures 30c and 34c.

These results are ascribed to the enhanced mass conservation across the interface ensured by these methods. Indeed, by monitoring the evolution of the vesicle area over time, Figure 35 shows minimal area changes with the FD-LJ and NXFEM methods, and significant convergence with the FD-GD method after reasonable grid refinement. Conversely, the FD method exhibits substantial vesicle area variation throughout the simulation at all grid levels, indicative of significant mass losses across the interface. Concurrently, it fails to accurately predict significant pressure jumps between the inner vesicle and the cavity, regardless of the refinement level used (see Figures 32b, 33b, 34b), resulting in poor interface position approximation (see Figures 29b, 30b, 31b). Figure 36 displays the trajectory of the vesicle point in position $\boldsymbol{x} = (0, 0)$ at $t = 0$. Notably, the trajectories of the FD-GD, FD-LJ, and NXFEM methods converge after appropriate grid refinement.

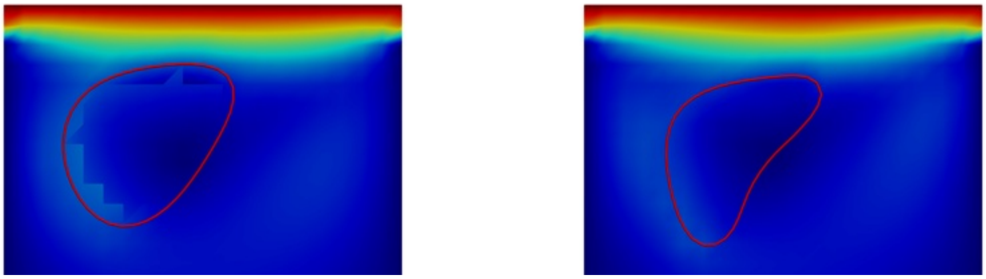

(a) NXFEM method.

(b) FD method.

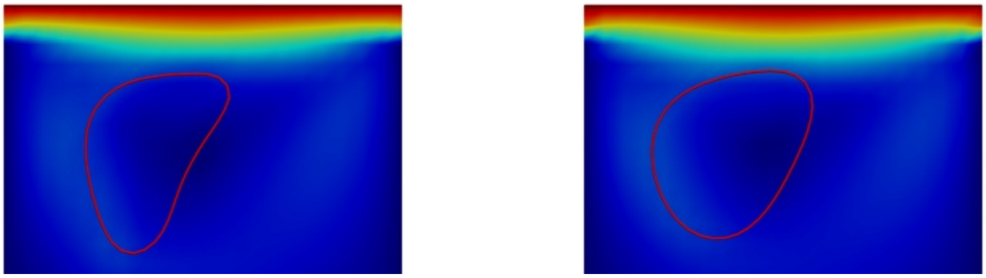

(c) FD-GD method.

(d) FD-LJ method.

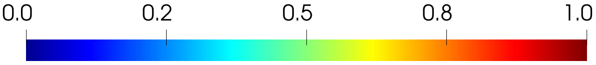

Figure 29: Snapshots of the fluid velocity magnitude at $t = 4.5$ for the *M1* refinement level.

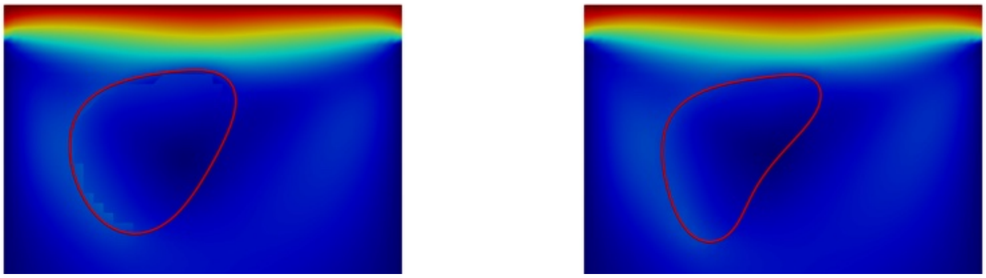

(a) NXFEM method.

(b) FD method.

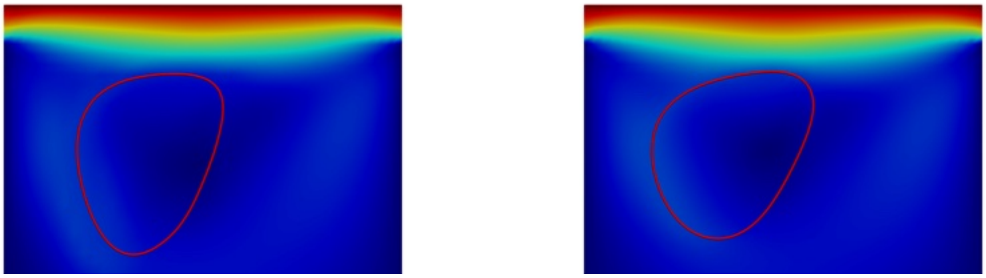

(c) FD-GD method.

(d) FD-LJ method.

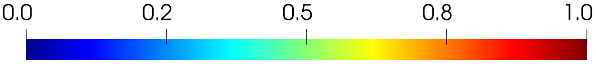

Figure 30: Snapshots of the fluid velocity magnitude at $t = 4.5$ for the *M2* refinement level.

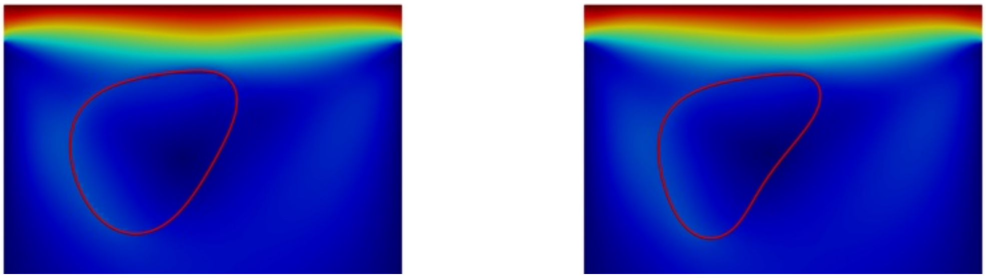

(a) NXFEM method.

(b) FD method.

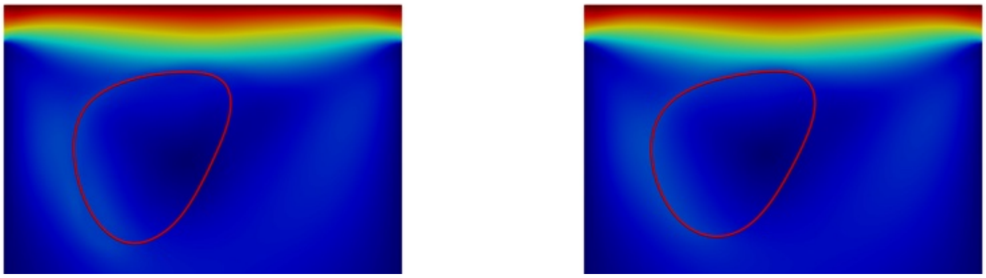

(c) FD-GD method.

(d) FD-LJ method.

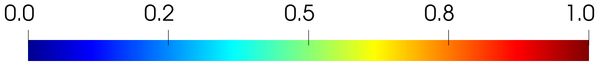

Figure 31: Snapshots of the fluid velocity magnitude at $t = 4.5$ for the *M3* refinement level.

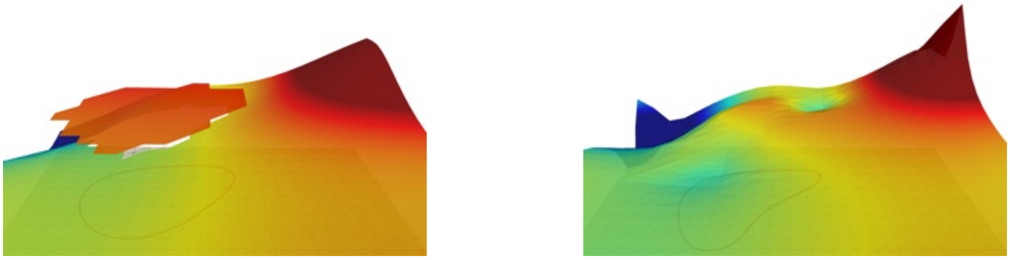

(a) NXFEM method.

(b) FD method

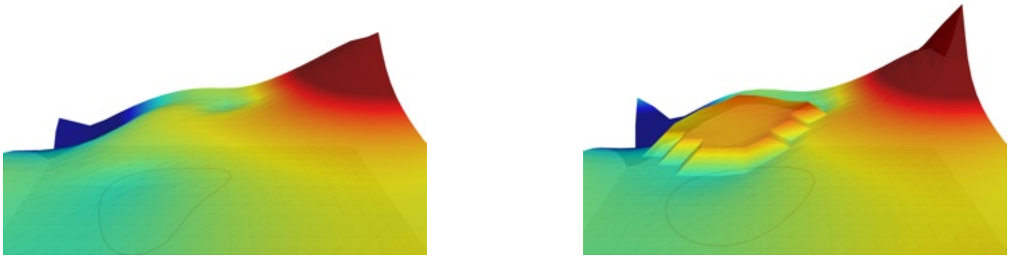

(c) FD-GD method.

(d) FD-LJ method.

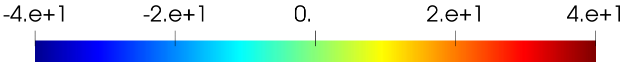

Figure 32: Snapshots of the fluid pressure at $t = 4.5$ for the *M1* refinement level.

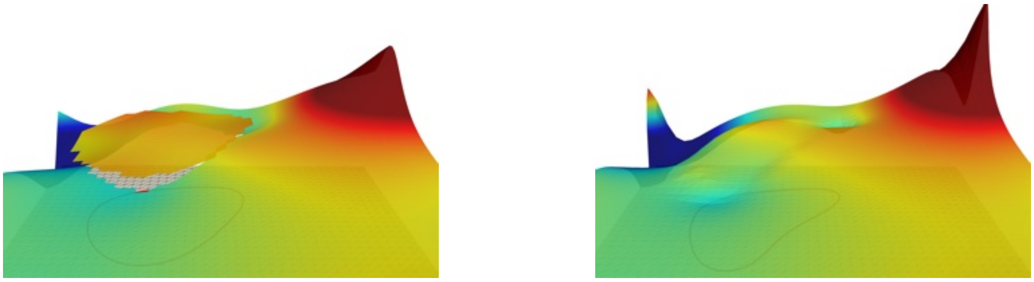

(a) NXFEM method.

(b) FD method.

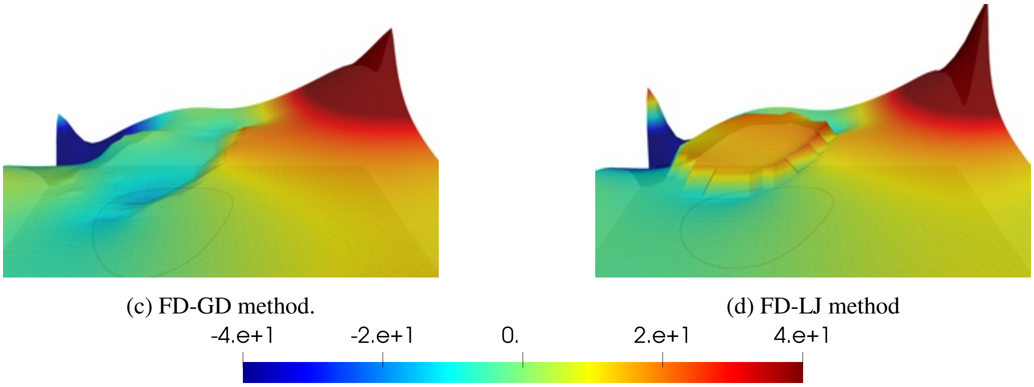

(c) FD-GD method.

(d) FD-LJ method

Figure 33: Snapshots of the fluid pressure at $t = 4.5$ for the *M2* refinement level.

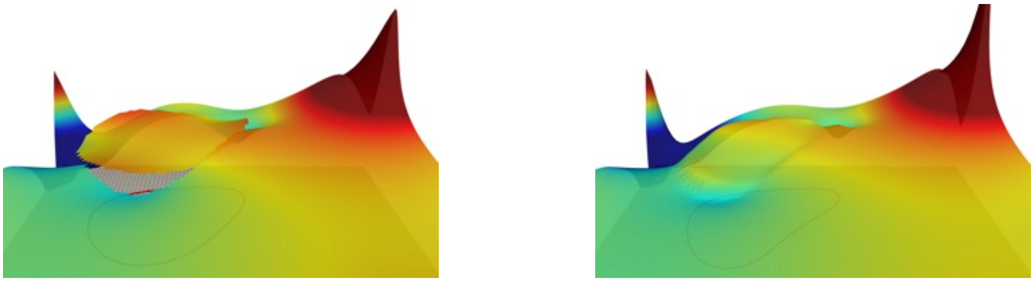

(a) NXFEM method.

(b) FD method.

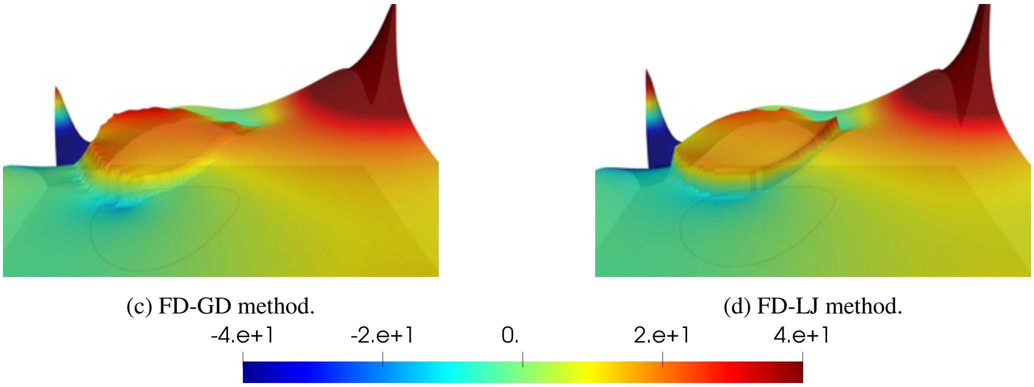

(c) FD-GD method.

(d) FD-LJ method.

Figure 34: Snapshots of the fluid pressure at $t = 4.5$ for the *M3* refinement level.

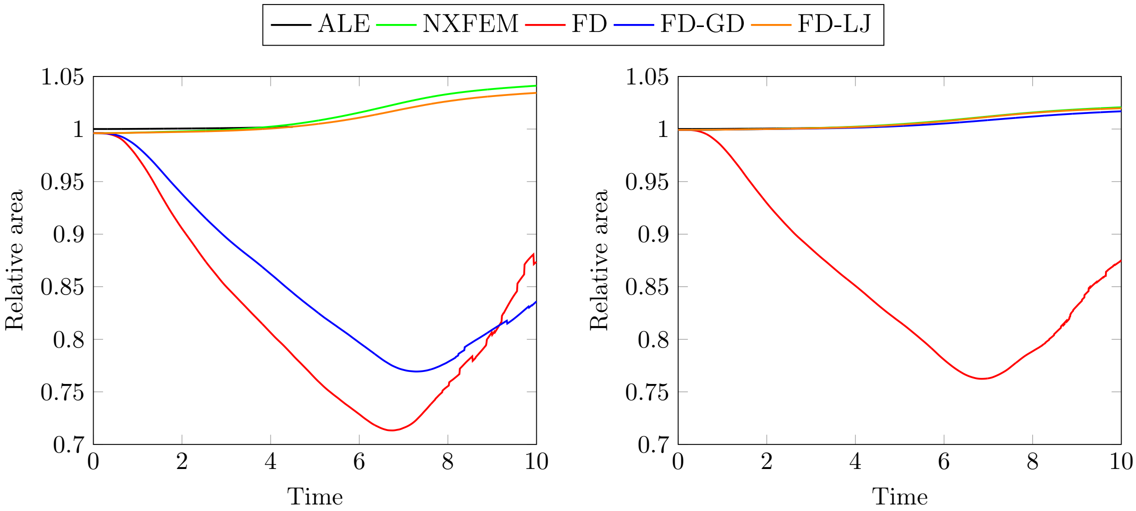

(b) *M1* vs. Reference.

(c) *M2* vs. Reference.

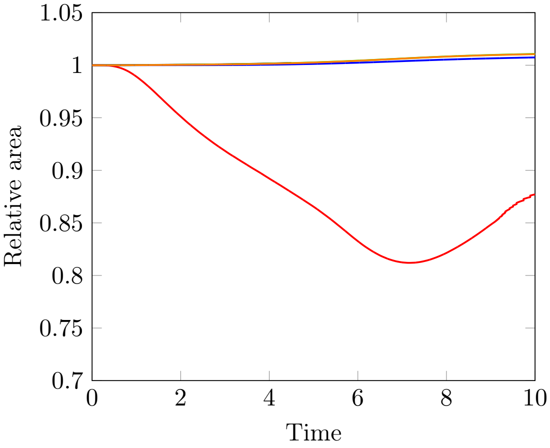

(d) *M3* vs. Reference.

Figure 35: Time history of the relative area of the vesicle.

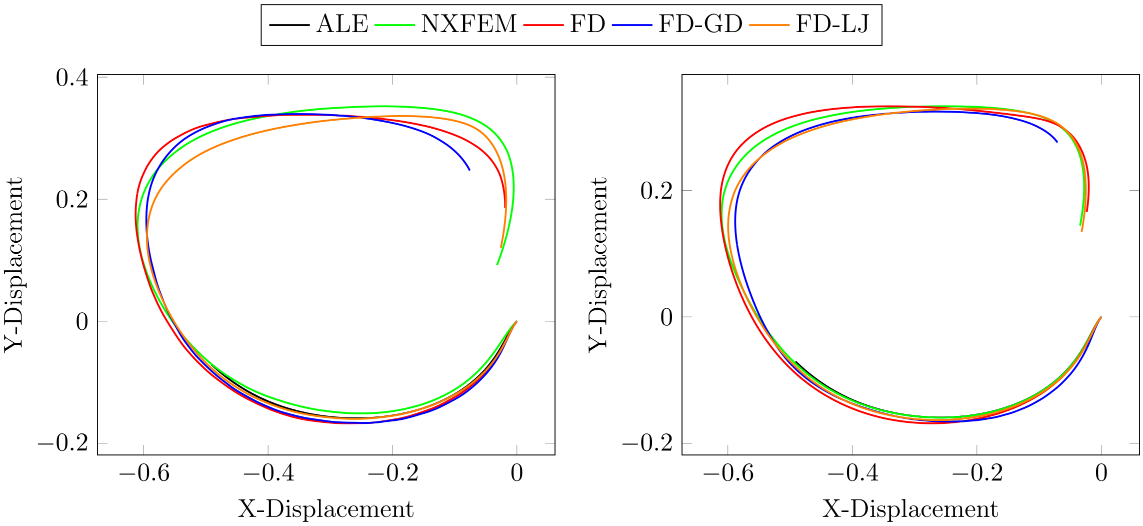

(b) *M1* vs. Reference.

(c) *M2* vs. Reference.

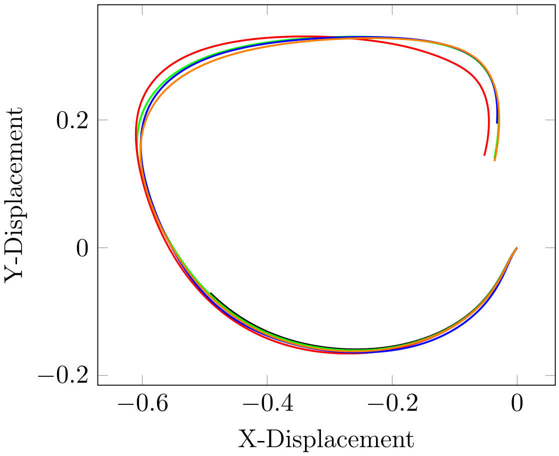

(d) *M3* vs. Reference.

Figure 36: Trajectory of the interface node initially located at $(0, 0)$.

4.2. Idealized 3D open valve

In this section, we assess the capabilities of Algorithm 1 in a 3D counterpart of the heart-valve inspired benchmark problem of Section 4.1.2. The primary goal is the numerical comparison of the two coupled models with different shell models presented in Sections 2.1.1 and 2.1.2.

All numerical simulations in this section are carried out using the `FELiScE` finite element library[2] for the fluid subproblem and the 2D-shell subproblem (4), alongside the `MoReFEM` finite element library[3] for the 3D-shell subproblem (2).

Geometrical setting. The fluid domain is defined as $\Omega = (0, 8)\times(0, 0.805)\times(0, 0.5)$, while the reference configuration of the shell is $\Omega^{\rm s} = (1.9894, 2.0106)\times(0, 0.7)\times(0, 0.5)$, with the mid-surface $\Sigma = \{2\}\times(0, 0.7)\times(0, 0.5)$.The depicted geometric configuration is illustrated in Figure 37. The simulation is conducted over a time interval $t \in [0, 3]$, which corresponds to three full oscillation cycles of the structure. Boundary conditions include a no-slip condition enforced on $\Gamma_{\rm wall}$, a symmetry condition on $\Gamma_{\rm sym}$ (bottom and lateral walls), zero traction on $\Gamma_{\rm out}$, and a prescribed parabolic profile on $\Gamma_{\rm in}$, given by:

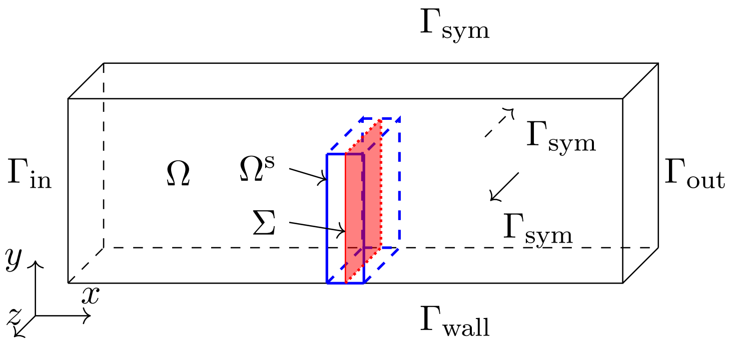

Figure 37: 3D idealized open valve geometric configuration.

$$\boldsymbol{u}(t) = -5y(1.61 - y)\,\mathrm{atanh}(5t)(\sin(2\pi t) + 1.1)\boldsymbol{n}.$$

The structure is clamped at its bottom with symmetry conditions prescribed on its lateral boundaries. Initially, both the fluid and structure are at rest. The physical parameters for the fluid in this test are: density $\rho^{\rm f} = 100$ and dynamic viscosity $\mu = 10$. For the structure, the parameters are: density $\rho^{\rm s} = 100$, thickness $\epsilon = 0.0212$, Young's modulus $E = 5.6 \cdot 10^7$, and Poisson's ratio $\nu = 0.4$.

Note that the parameters correspond to those used in Section 4.1.2, while Ω and Σ represent the extrusion in the z direction of the respective domains employed in the same section.

Spatial and temporal discretization. The domain Ω is represented by an unstructured simplicial mesh comprising 102150 elements, while the domain $\Omega^{\rm s}$ is defined using a structured grid composed of 70 tensorial shell elements. As a result, the mid-surface Σ is discretized with 140 triangular elements. Both the fluid and structure meshes are characterized by a spatial discretization parameter, h and $\mathcal{H}$ respectively, approximately equal to 0.11. The time-step used is $\tau = 1 \times 10^{-3}$. For the fitted mesh ALE method, which serves as reference solution, the fluid mesh consists of 173400 tetrahedra, while the solid mesh comprises 280 elements, with an average element size $h \approx 0.05$. Additionally, the stabilization parameters are chosen as $\gamma_{\rm p} = 1$ and $\gamma_{\rm d} = 0$ in (12), and $\gamma_\lambda = 10$ in (13). At every time step n, the subdomains Ω_1^n and Ω_2^n are identified to define the approximation space Q^n using a fictitious interface $\Sigma_{\rm fic}^n$. This interface is derived by projecting, at each time step, the immersed upper boundary of Σ onto the boundary $\Gamma_{\rm top}$, as depicted in Figure 39. This interface is an extrusion in the z-axis direction of the interface $\Sigma_{\rm fic}^n$ illustrated in Figure 17.

Comparison of the results. As in the 2D case, the oscillatory velocity profile induces a periodic deflection of the solid. Owing to the symmetry of the setting, the solution is invariant along the z-direction. To conduct a comparative

---

[2] `https://gitlab.inria.fr/felisce/felisce`

[3] `https://gitlab.inria.fr/MoReFEM`

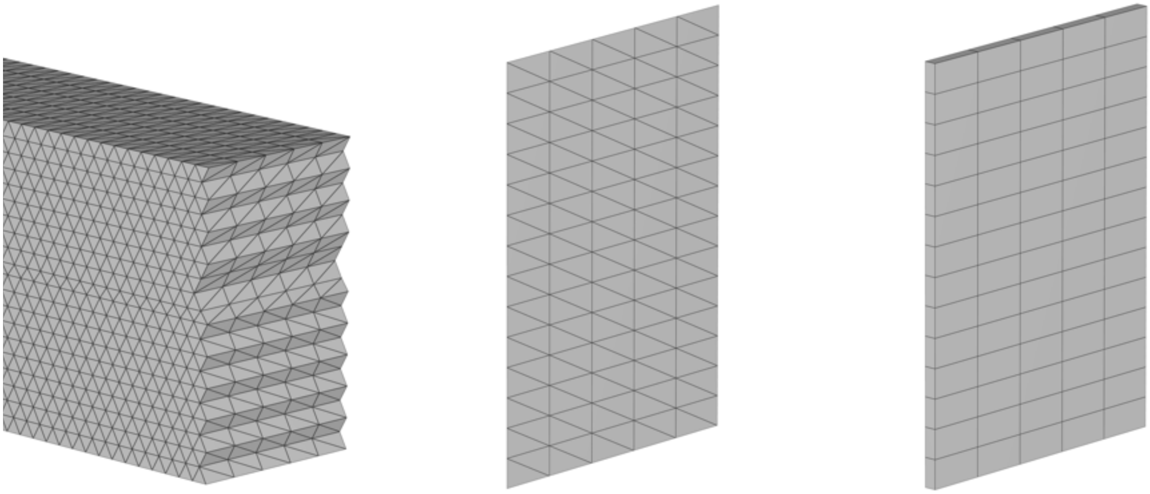

(a) Section of the fluid domain mesh.

(b) Mesh of the solid domain mid-surface.

(c) Mesh of the solid domain.

Figure 38: Fluid and solid meshes.

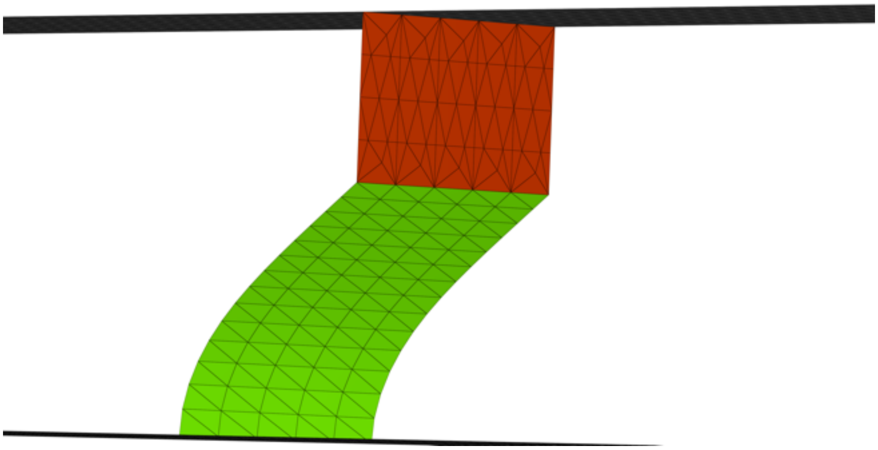

Figure 39: Representation of the solid mid-surface Σ^n in green and the fictitious interface Σ^n_{fic} in red.

analysis, we focus on the time instant $t = 0.5$, coinciding with the moment when the valve reaches its maximum displacement. Figure 40 shows the reference solution obtained with fitted mesh ALE approach. However, it is necessary to use this reference solution with caution, as a significant impact of mesh distortion on the numerical solution is observed. Figure 41 presents the numerical solution obtained with Algorithm 1 and the two different shell models. By comparing with Figure 40, we observe that Algorithm 1 provides a good approximation for a relatively coarse mesh, although the maximum velocity magnitude is slightly lower than the reference solution. Nonetheless, considering the exceedingly coarse mesh utilized for the discretization of the structure (the solid mesh dimension $\mathcal{H}$ is twice as large as the one employed in Section 4.1.2 for the *M1* refinement level), the obtained result is considered as satisfactory. Figure 42 illustrates a comparison of the temporal evolution of displacement in the x and y directions

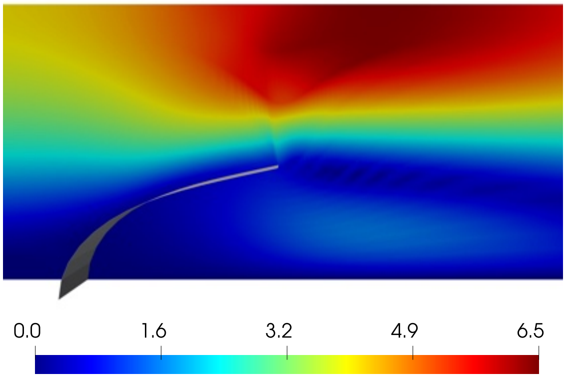

Figure 40: Snapshot of the velocity magnitude at $t = 0.5$ for the reference solution.

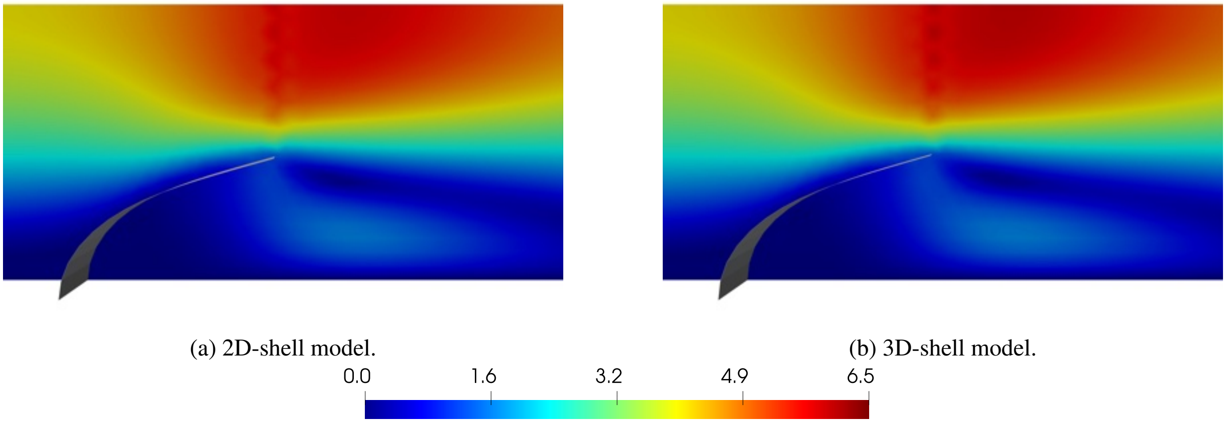

(a) 2D-shell model.

(b) 3D-shell model.

Figure 41: Snapshots of the fluid velocity magnitude at $t = 0.5$.

at the midpoint of the upper leaflet edge. Initially, the proposed fictitious domain method shows good alignment with the ALE method, although it slightly diverges when the structure reaches its maximum bending level (see Figure 42). Additionally, Figure 42 clearly illustrates the two shell formulations yielding similar results for this test case. Moreover, it is worth noting that the reference solution is obtained using a 2D-shell model, which may account for the slightly better agreement observed between the 2D-shell model with Algorithm 1 and the fitted mesh ALE approach.

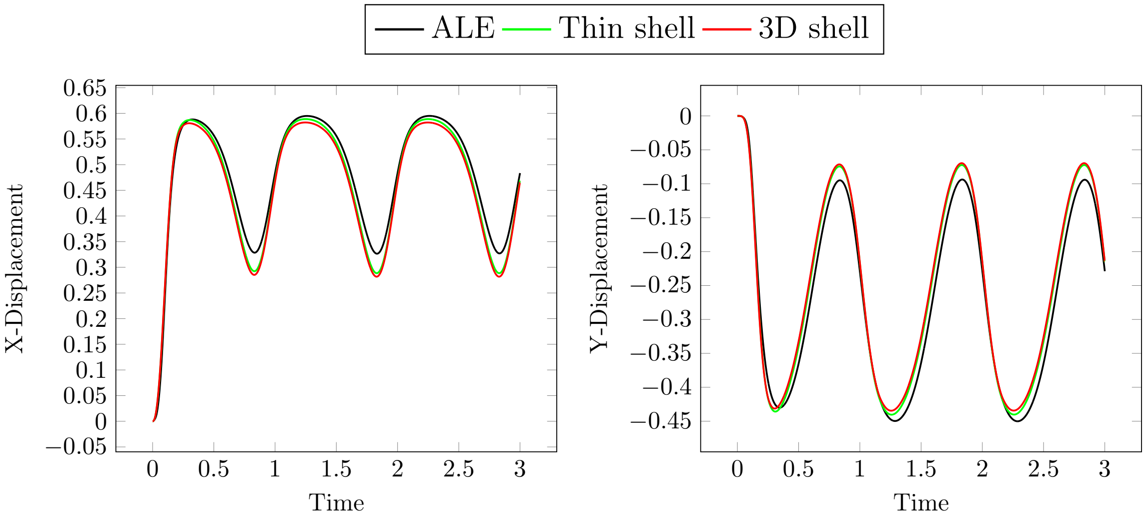

(b) x-displacement.

(c) y-displacement.

Figure 42: Time history of the x-displacement (left) and y-displacement (right) of the mid-point of the valve end-edge.

4.3. Aortic valve with contact

In this section, we investigate the capabilities of Algorithm 1 to simulate the dynamics of the aortic valve over a complete cardiac cycle. In particular, we assess the impact of enhanced mass conservation by comparing the results obtained using Algorithm 1 with those obtained removing the additional mass conservation constraint from it, i.e. by considering $p_h, q_h \in \widetilde{Q}$ in (17). Hereafter, we refer to these two methods as the FD-LJ method and the FD-LG method, respectively. Simulating the FSI of the aortic valve presents several challenges. One notable difficulty arises from the large deformations and fast dynamics of the valve during opening and closing phases. Specifically during the closing phase, employing contact algorithms is crucial to prevent leaflet interpenetration. Additionally, when the valve is closed, it experiences substantial pressure drops, underscoring the importance of preventing mass leakage to ensure the reliability and accuracy of the results.

The numerical simulations in this section were conducted using the `FELiScE` finite element library[4] for the fluid subproblem and the `MoReFEM` finite element library[5] for the structural subproblem.

Geometrical setting. The aortic root, located between the outflow tract of the left ventricle and the ascending aorta, contains the aortic valve. Specifically, it extends from the superior sinotubular junction to the inferior bases of the valve leaflets. Notably, the aortic root features three sinuses, expanses defined proximally by the attachments of the valve leaflets and distally by the sinotubular junction.

In modeling this anatomical region, we consider the domain Ω as a circular rigid tube with a diameter and length of approximately 2cm, which incorporates the three-lobed dilation of the sinuses near the valve (see Figure 43a). The geometry of the aortic valve with its three leaflets (although, in pathological cases, they may reduce to two) is represented in Figure 43c. The temporal domain encompasses $t \in [0, 0.342]$, corresponding to a single cycle (opening and closure).

We define the inflow and outflow boundaries as the bases of the domain Ω lying on the ventricular and aortic sides, respectively (i.e.the bottom and top bases in Figure 43a). At the inflow boundary, denoted as Γ_{in}, we prescribe the idealized left ventricular pressure profile illustrated in Figure 44 and adapted from [41]. Conversely, at the outflow boundary, denoted as Γ_{out}, we apply the resistance boundary condition $\boldsymbol{\sigma}^f(\boldsymbol{u}, p)\boldsymbol{n} = -(p_0 + RQ)\boldsymbol{n}$, where $p_0 = 80$mmHg represents a constant physiological pressure level, Q denotes the volumetric flow rate through the outflow (with the convention that $Q > 0$ indicates flow leaving the domain), $R = 70(\text{dyn} \cdot \text{s})/\text{cm}^5$ is a resistance constant (see [41]). These parameters ensure a realistic transvalvular pressure difference of 80mmHg during the diastolic steady state (where Q is nearly zero), while permitting a reasonable flow rate during systole. On the wall of the aortic root, denoted

---

[4] `https://gitlab.inria.fr/felisce/felisce`

[5] `https://gitlab.inria.fr/MoReFEM`

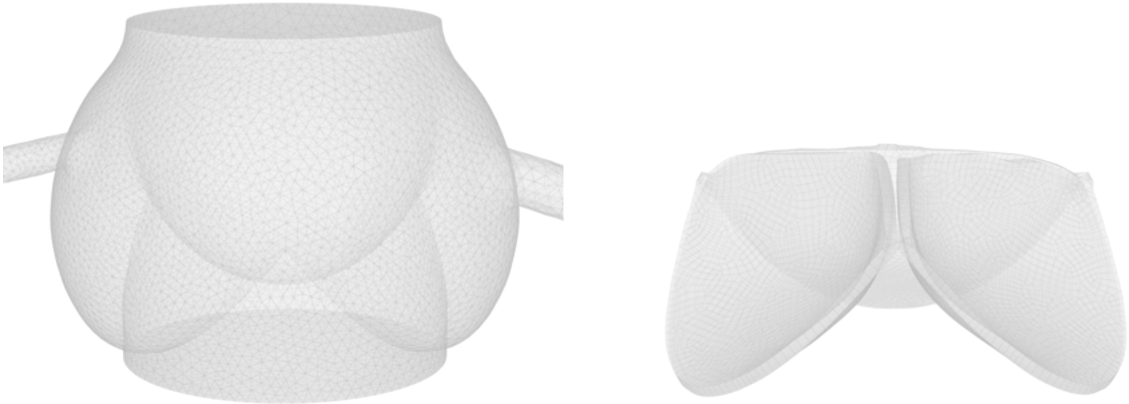

(a) Aortic root domain.

(b) Aortic valve domain.

(c) Aortic valve mid-surface.

Figure 43: Geometric description and computational meshes.

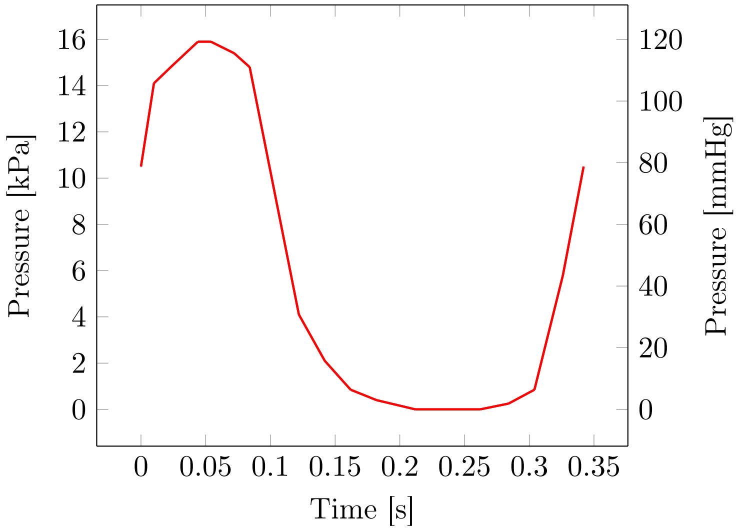

Figure 44: Idealized left ventricular (LV) pressure profile applied to the inflow boundary Γ_{in} (see [41])

by Γ_w, we impose the no-slip boundary condition $\boldsymbol{u} = \boldsymbol{0}$. Backflow stabilization is applied both on Γ_{in} and Γ_{out} to avoid the traditional instability issues of the Navier-Stokes approximations with Neumann boundary conditions (see, e.g., [7]). At time $t = 0$, the system is at rest; notably, the inflow pressure condition on Γ_{in} of Figure 44 coincides with p_0.

The fluid parameters, which reflect the physical properties of human blood (see, e.g., [42, 56]), are defined as $\rho^f = 1.0\text{g}/\text{cm}^3$ and $\mu = 3 \cdot 10^{-2}\text{g}/(\text{cm} \cdot \text{s})$. For the valve leaflets, we adopt an isotropic St. Venant–Kirchhoff material model with $E = 1 \cdot 10^7 \text{dyn}/\text{cm}^2$ and $\nu = 0.499$. The solid density is $\rho^s = 1.2\text{g}/\text{cm}^3$, and the thickness of the leaflets is approximately $\epsilon = 3.86 \cdot 10^{-2}\text{cm}$.

Spatial and temporal discretization. The domain Ω is discretized using a simplicial mesh comprising 297, 822 tetrahedral elements, with each element having a characteristic size of approximately $h \approx 0.09$. For the valve, the 3D-shell model detailed in Section 2.1.1 is employed. The valve domain Ω^s is constituted of 4, 472 shell elements, as depicted in Figure 5. The valve mid-surface Σ, utilized for enforcing the FSI coupling conditions and the contact penalty term, is represented by a 3D surface mesh composed of 8, 944 triangles and fitted to Ω^s with an approximate characteristic size of $\mathcal{H} \approx 0.7$. The time step chosen for the simulation is $\tau = 10^{-4}$s. Additionally, we set $\gamma_p = 1$ and $\gamma_d = 0$ in equation (12). In equation (13), the parameter γ_λ is assigned a value of 10^3. The contact penalty parameter $\kappa_c = 5 \cdot 10^7$, while the contact relaxation parameter $\varepsilon_g = 2 \cdot 10^{-2}$cm.

At each time step n, a fictitious interface Σ^n_{fic} is employed in order to identify the two subdomains Ω^n_1 and Ω^n_2 used for defining the pressure approximation space Q^n. The corresponding triangulation $\mathcal{T}_{\mathcal{H}}^{\Sigma^n_{\text{fic}}}$ is constructed following the steps outlined in Algorithm 2 and illustrated in Figure 45.

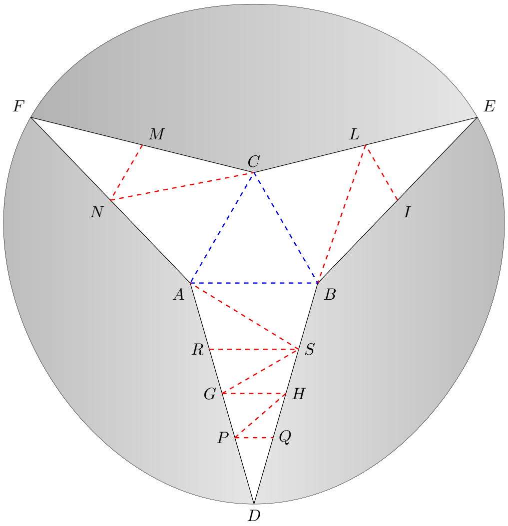

Figure 45: Schematic representation of the construction of the fictitious interface Σ_{fic}. Top view of the aortic valve. In *gray* the valve leaflets.

Figure 46 illustrates the fictitious interface generated by Algorithm 2 at three different time steps. It is important to note that no unknowns are defined on this mesh; it is solely used for integration purposes. Algorithm 2 is implemented within the software `Wolf` [6].

Comparison of the results. The numerical simulation starts almost at the beginning of the systolic phase, precisely at the conclusion of the isovolumetric ventricular contraction. During this phase, as the ventricular pressure steadily increases, the aortic valve begins to open, allowing blood flow from the left ventricle into the aorta. As the blood is propelled into the aorta, the ventricular pressure gradually decreases until it falls below the aortic pressure, resulting in a slight backward flow. This backward flow prompts the closure of the aortic valve, vanishing with it. Subsequently, the diastolic phase begins, with the left ventricle and the aorta separated by the closed aortic valve, and only minimal blood recirculation on both sides of the valve is experienced. The ventricular pressure then resumes increasing, marking the beginning of a new cardiac cycle.

---

[6] `https://gitlab.inria.fr/alauzet/wolf`

Algorithm 2: Triangulation of the fictitious interface Σ^n_{fic}, as shown in Figure 45.

```
Input: $\Sigma^n_{\text{fic}}$ boundary edges.
    1. Add the central triangle $ABC$ to $\mathcal{T}_{\mathcal{H}}^{\Sigma^n_{\text{fic}}}$.
    2. Starting from edge $BA$, consider vertices $R$ and $S$ to form triangles $BAR$ and $BAS$. Select the triangle with higher quality, e.g., $BAS$, and add it to $\mathcal{T}_{\mathcal{H}}^{\Sigma^n_{\text{fic}}}$.
    3. Starting from edge $SA$, consider vertices $R$ and $H$ to form triangles $SAR$ and $SAH$. Again, select the triangle with higher quality, e.g., $SAR$, and add it to $\mathcal{T}_{\mathcal{H}}^{\Sigma^n_{\text{fic}}}$.
    4. Repeat step (3) for edge $SR$ to obtain $SRC$, for edge $SC$ to obtain $SCH$, etc.
    5. From edge $QP$, the only available vertex is $D$. Add the triangle to $\mathcal{T}_{\mathcal{H}}^{\Sigma^n_{\text{fic}}}$.
    6. Finally the obtained triangulation is appropriately refined.
Output: Triangulation $\mathcal{T}_{\mathcal{H}}^{\Sigma^n_{\text{fic}}}$.
```

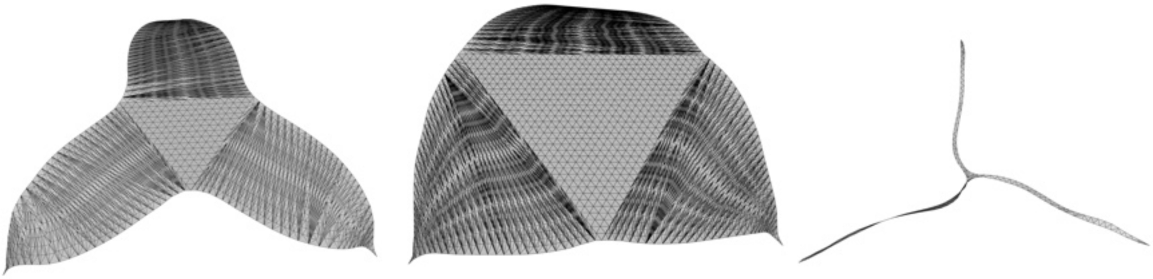

(a) $t = 0.015$. (b) $t = 0.080$. (c) $t = 0.250$.

Figure 46: Fictitious interface generated by Algorithm 2 at different time steps.

Figures 48 and 47 provide some snapshots of the fluid velocity field and the mid-surface valve deformation, respectively, captured at different time instances for both the FD-LJ and FD-LG approaches. Notably, the FD-LJ method demonstrates superior interfacial mass conservation compared to the FD-LG method.

In particular, for the FD-LG method, significant spurious velocity and a lack of mass conservation are observed across the valve leaflets during the initial stages of valve opening ($t = 0.015$), in contrast to the behavior exhibited by the FD-LJ method (see Figures 48a-b). As a result, the fluid-induced stress on the valve leaflets is lower with the FD-LG method compared to the FD-LJ method, leading to reduced leaflet displacement (see Figures 47a-b). The discrepancy in valve displacement between the two methods is evident throughout the entire simulation, with a more pronounced contrast observed during the transition between the open and closed configurations (refer to Figures 47a-b-e-f). Even at maximum valve opening, this difference persists, with the valve position slightly more closed in the FD-LG method compared to the FD-LJ method (see Figures 47c-d).

At this point, Figures 48c-d show a significant blood flow from the left ventricle into the aorta, i.e., from Γ_{in} to Γ_{out}. Although the FD-LJ method demonstrates enhanced mass conservation compared to the FD-LG method, both methodologies reveal some degree of mass leakage near the valve attachment to the aortic root wall. Notably, this leakage is less pronounced when utilizing the FD-LJ approach. The emergence of this spurious velocity is attributed to the relatively coarse resolution and is expected to diminish with increased levels of refinement.

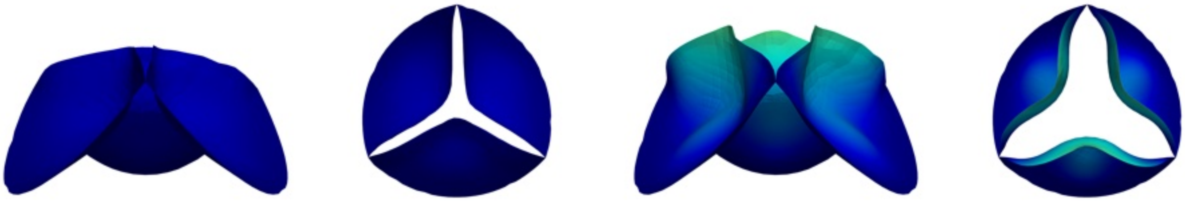

(a) $t = 0.015$, FD-LG method.

(b) $t = 0.015$, FD-LJ method.

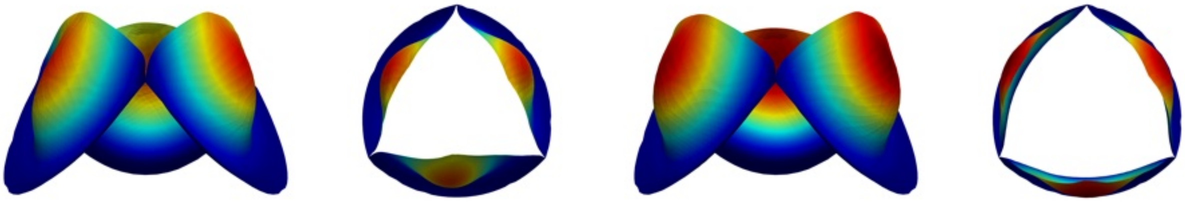

(c) $t = 0.080$, FD-LG method.

(d) $t = 0.080$, FD-LJ method.

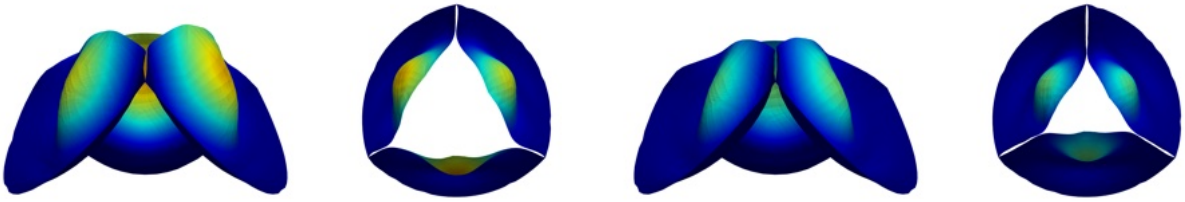

(e) $t = 0.112$, FD-LG method.

(f) $t = 0.112$, FD-LJ method.

Figure 47: Snapshots of the valve deformation from two perspectives: top view and side view, colored by displacement magnitude.

During the closure phase, a flow is observed from Γ_{out} to Γ_{in} owing to the higher pressure in the aorta compared to the ventricle (see Figures 48e-f). As the valve gradually closes, the enhanced mass conservation offered by the FD-LJ method becomes more prominent. Under these circumstances, the velocity field is expected to gradually decrease, eventually showing only minimal recirculation phenomena on each side of the valve when the valve is fully closed. However, with the FD-LG method, significant velocity fields persist, resulting in substantial mass leakage (see Figures 48h-j), whereas the FD-LJ demonstrates a gradual reduction of blood recirculation after an initial transition period (see Figures 48i-k). In particular, the presence of spurious velocity in the FD-LG leads to a non-natural twisting motion (see Figure 47e), causing partial detachment of the leaflets and the formation of space, resulting in induced blood flow across the valve.

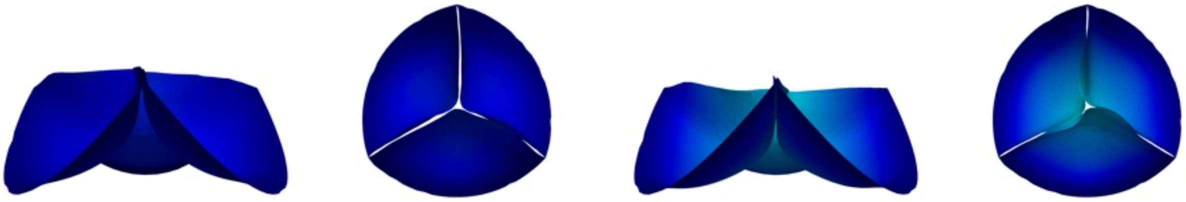

(h) $t = 0.142$, FD-LG method.

(i) $t = 0.142$, FD-LJ method.

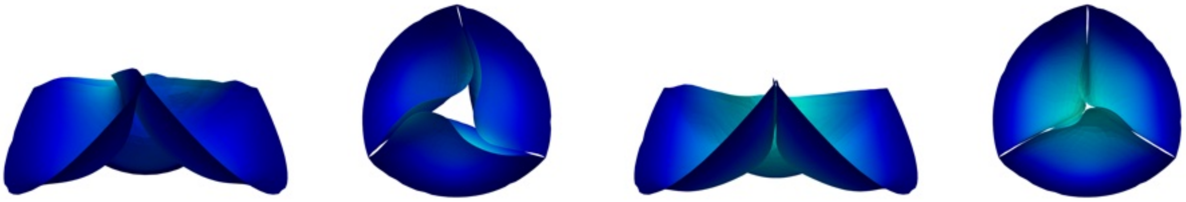

(j) $t = 0.250$, FD-LG method.

(k) $t = 0.250$, FD-LJ method.

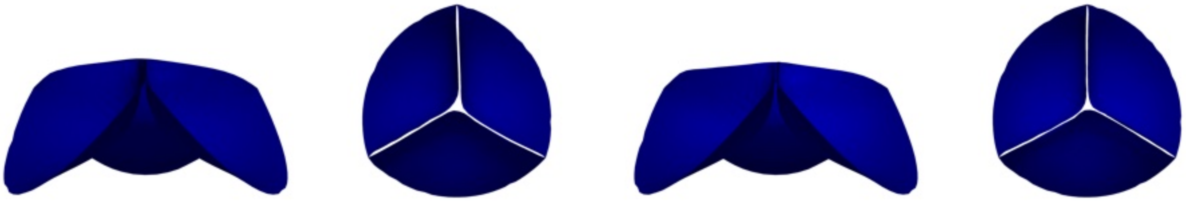

(l) $t = 0.342$, FD-LG method.

(m) $t = 0.342$, FD-LJ method.

Figure 47: Snapshots of the valve deformation from two perspectives: top view and side view, colored by displacement magnitude.

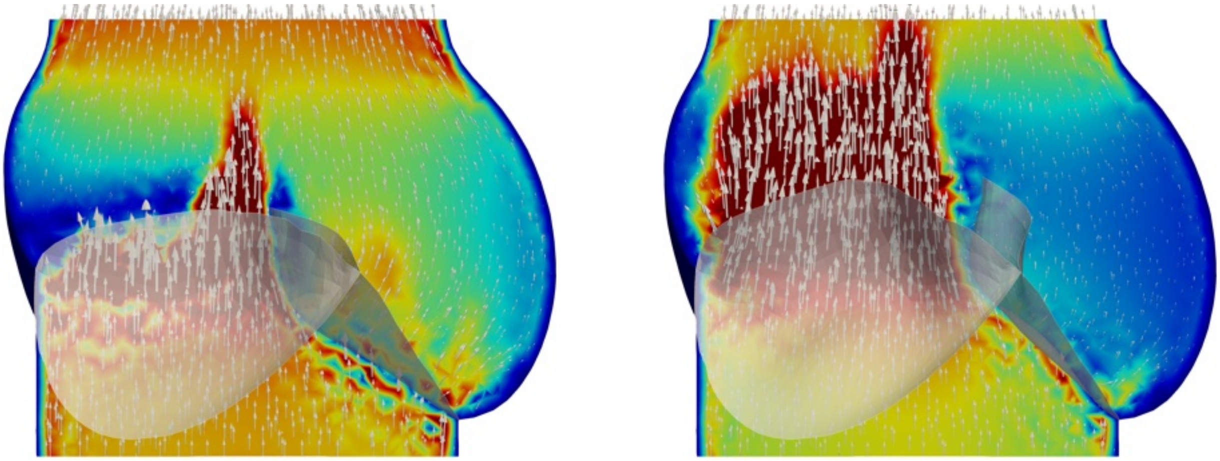

(a) $t = 0.015$, FD-LG method.

(b) $t = 0.015$, FD-LJ method.

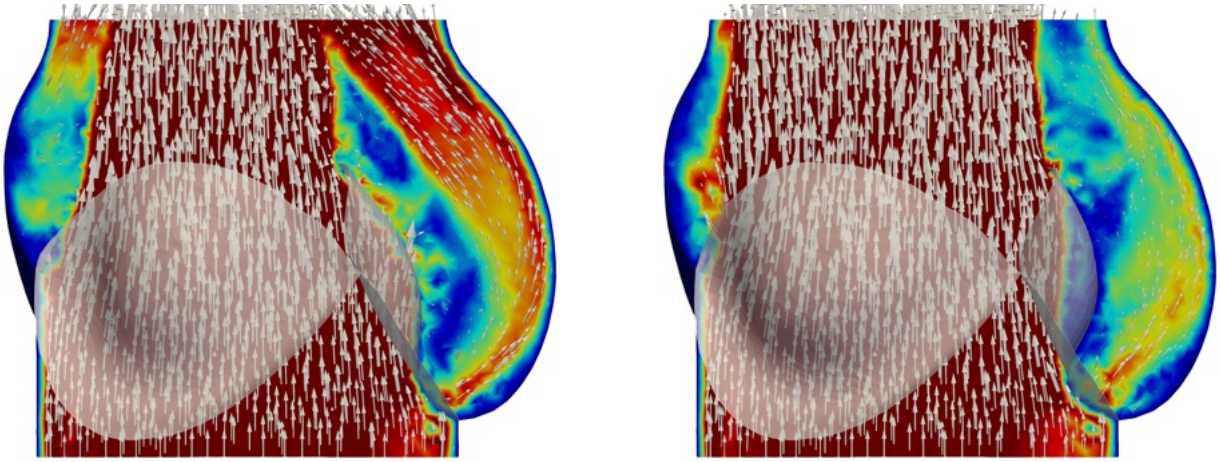

(c) $t = 0.080$, FD-LG method.

(d) $t = 0.080$, FD-LJ method.

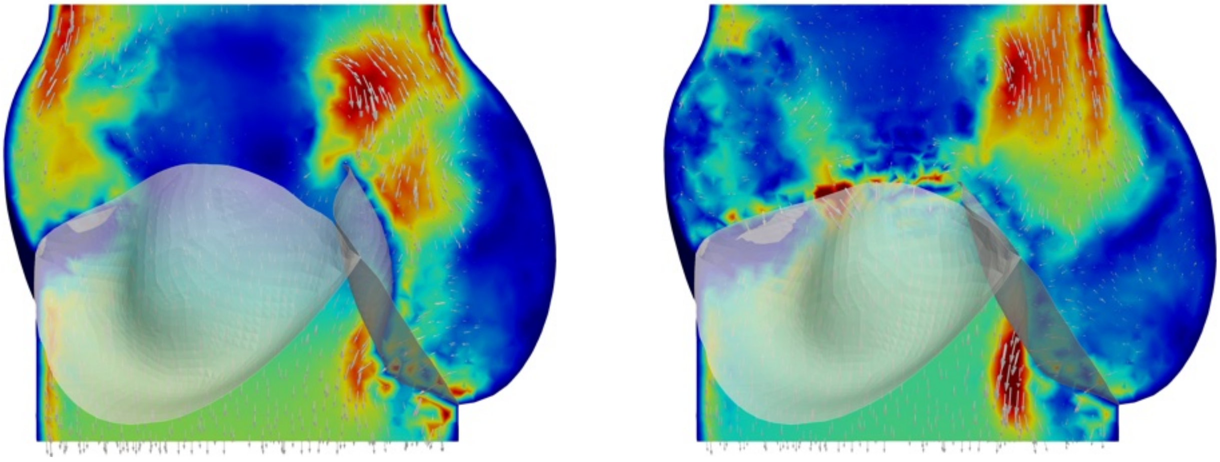

(e) $t = 0.112$, FD-LG method.

(f) $t = 0.112$, FD-LJ method.

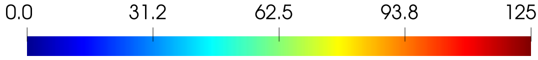

Figure 48: Snapshots of the fluid velocity field at multiple time steps throughout a cardiac cycle. Left: Results obtained using the FD-LG method. Right: Results obtained using the FD-LJ method

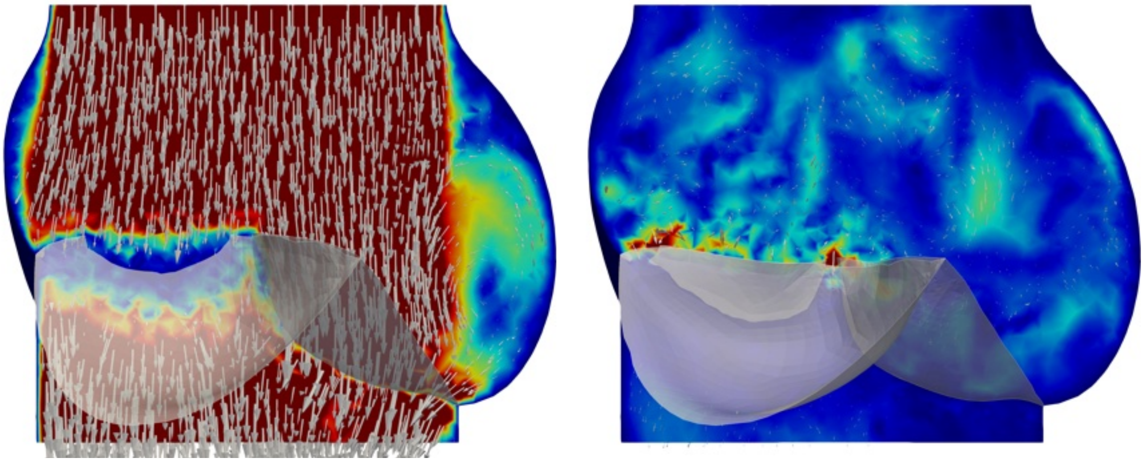

(h) $t = 0.142$, FD-LG method.

(i) $t = 0.142$, FD-LJ method.

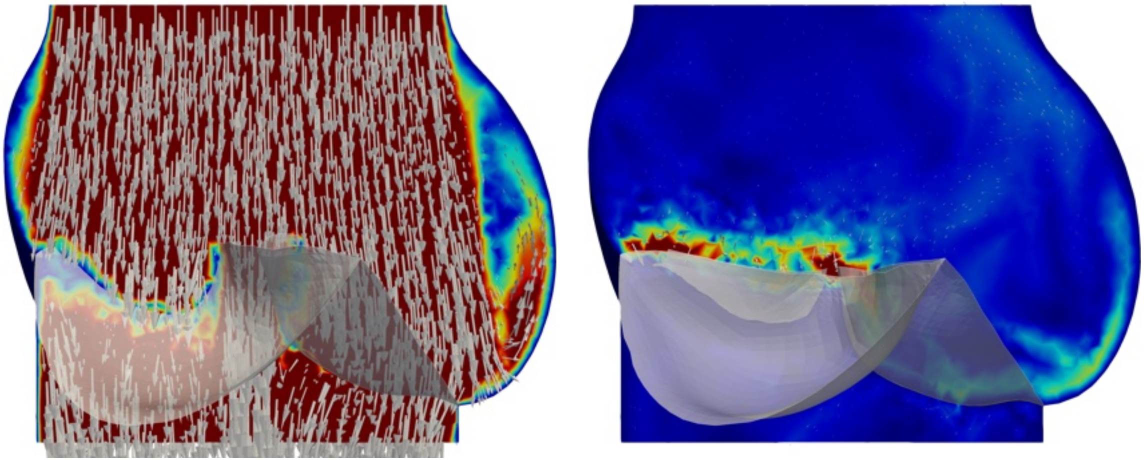

(j) $t = 0.250$, FD-LG method.

(k) $t = 0.250$, FD-LJ method.

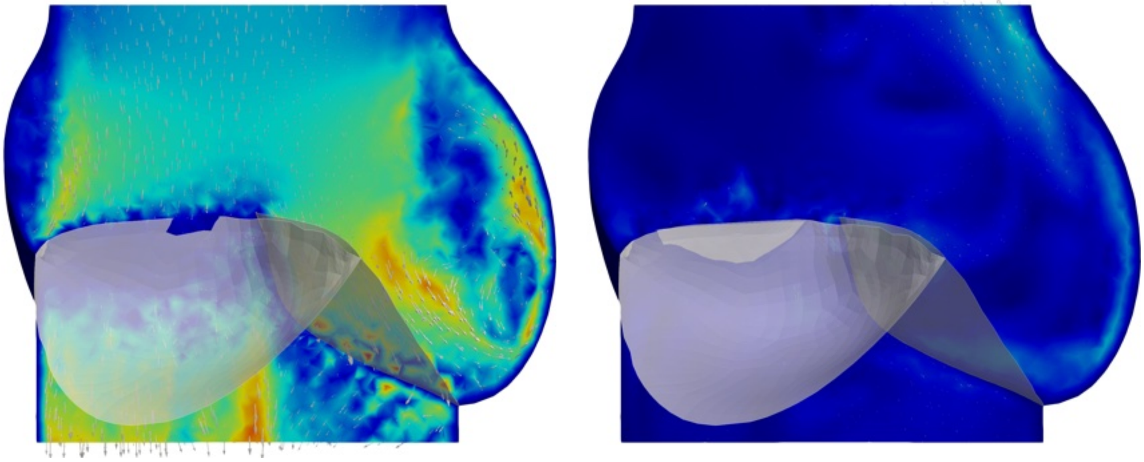

(l) $t = 0.342$, FD-LG method.

(m) $t = 0.342$, FD-LJ method.

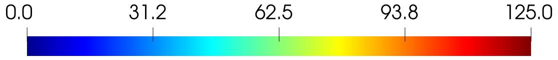

Figure 48: Snapshots of the fluid velocity field at multiple time steps throughout a cardiac cycle. Left: Results obtained using the FD-LG method. Right: Results obtained using the FD-LJ method.

Figures 48i-k show minor fluid leakage along the contact region between the valve leaflets. This leakage is ascribed to the contact relaxation parameter ϵ_{g} employed in the contact algorithm to avoid penetration. Nonetheless, decreasing the value of the contact relaxation parameter ϵ_{g} is expected to mitigate this phenomenon. Figures 48l-m, captured at the initial stage of the valve opening phase, exhibit similar trends to those observed at previous time instances for both methods.

5. Conclusion

We have proposed a fictitious domain method for immersed FSI with enhanced mass conservation based on the symmetric variant of the method presented in [24]. The behavior of the immersed thin-walled structure was modeled using both 2D and 3D-shell models. A salient feature of the proposed method is that the size of the system matrix remains constant regardless of the location of the interface with respect to the background computational mesh, which is particularly advantageous for cases involving moving interfaces. This innovative fictitious domain method for immersed fluid-structure interaction has been compared and validated through a series of 2D benchmarks, encompassing fully non-linear models and large interface deflections, alongside alternative numerical approaches. The proposed approach demonstrates similar or superior accuracy compared to alternative fictitious domain methods. Notably, it achieves this without the necessity of resorting to penalty terms, which can compromise the conditioning of the resulting system matrix. Furthermore, the accuracy achieved is comparable to that of the Nitsche-XFEM method, provided a reasonable level of mesh refinement is used. In the numerical test under consideration, both shell models produce comparable results; however, the 3D-shell formulation offers distinct advantages. Notably, it facilitates coupling with other 3D media, e.g., the aortic valve with the left ventricle, enables the use of arbitrary 3D material laws, and provides more precise information throughout the body's thickness. Finally, the method has been successfully applied to the simulation of the aortic valve under realistic conditions. The improvement in mass conservation ensured by the proposed method is notably evident when the valve is closed, in contrast to the standard fictitious domain method, leading to an overall satisfactory solution.

Acknowledgement

This work was funded by the French National Research Agency (ANR), through the SIMR project (ANR-19-CE45-0020). The authors also thank Frédéric Alauzet (Inria) for the inspiring discussions on the triangulation of the fictitious interface.

References

[1] F. Alauzet, B. Fabrèges, M. A. Fernández, and M. Landajuela. Nitsche-XFEM for the coupling of an incompressible fluid with immersed thin-walled structures. *Computer Methods in Applied Mechanics and Engineering*, 301:300–335, 2016.

[2] Frédéric Alauzet. A changing-topology moving mesh technique for large displacements. *Engineering with Computers*, 30(2):175–200, 2014.

[3] M. Astorino, J.-F. Gerbeau, O. Pantz, and K.-F. Traore. Fluid–structure interaction and multi-body contact: application to aortic valves. *Computer Methods in Applied Mechanics and Engineering*, 198(45-46):3603–3612, 2009.

[4] Frank P. T. Baaijens. A fictitious domain/mortar element method for fluid–structure interaction. *International Journal for Numerical Methods in Fluids*, 35(7):743–761, 2001.

[5] K.J. Bathe. *Finite Element Procedures*. Prentice Hall, 1996.

[6] M. Bergmann, A. Fondanèche, and A. Iollo. An Eulerian finite-volume approach of fluid-structure interaction problems on quadtree meshes. *Journal of Computational Physics*, 471:111647, 2022.

[7] Cristóbal Bertoglio, Alfonso Caiazzo, Yuri Bazilevs, Malte Braack, Mahdi Esmaily, Volker Gravemeier, Alison L. Marsden, Olivier Pironneau, Irene E. Vignon-Clementel, and Wolfgang A. Wall. Benchmark problems for numerical treatment of backflow at open boundaries. *International Journal for Numerical Methods in Biomedical Engineering*, 34(2):e2918, 2018.

[8] M. Bischoff, K.U. Bletzinger, W.A. Wall, and E. Ramm. Models and finite elements for thin-walled structures. In *Encyclopedia of Computational Mechanics*, chapter 2. John Wiley & Sons, 2004.

[9] D. Boffi, N. Cavallini, F. Gardini, and L. Gastaldi. Local mass conservation of Stokes finite elements. *Journal of Scientific Computing*, 52:383–400, 2012.

[10] D. Boffi, N. Cavallini, F. Gardini, and L. Gastaldi. Stabilized Stokes elements and local mass conservation. *Bollettino dell'Unione Matematica Italiana*, 5(3):543–573, 2012.

[11] D. Boffi, N. Cavallini, and L. Gastaldi. Finite element approach to immersed boundary method with different fluid and solid densities. *Mathematical Models and Methods in Applied Sciences*, 21(12):2523–2550, 2011.

[12] D. Boffi and L. Gastaldi. A fictitious domain approach with Lagrange multiplier for fluid-structure interactions. *Numerische Mathematik*, 135(3):711–732, 2017.

[13] Daniele Boffi, Nicola Cavallini, and Lucia Gastaldi. The finite element immersed boundary method with distributed Lagrange multiplier. *SIAM Journal on Numerical Analysis*, 53(6):2584–2604, 2015.

[14] L. Boilevin-Kayl, M. A. Fernández, and J.-F. Gerbeau. Numerical methods for immersed FSI with thin-walled structures. *Computers & Fluids*, 179:744–763, 2019.

[15] E. Burman and P. Hansbo. Fictitious domain methods using cut elements: III. A stabilized Nitsche method for Stokes' problem. *ESAIM: Mathematical Modelling and Numerical Analysis*, 48:497–514, 2014.

[16] E. Burman, P. Hansbo, and M. G. Larson. Cut finite element method for divergence free approximation of incompressible flow: optimal error estimates and pressure independence, 2022.

[17] Erik Burman and Miguel A. Fernández. An unfitted Nitsche method for incompressible fluid–structure interaction using overlapping meshes. *Computer Methods in Applied Mechanics and Engineering*, 279:497–514, 2014.

[18] H. Casquero, C. Bona-Casas, and H. Gomez. NURBS-based numerical proxies for red blood cells and circulating tumor cells in microscale blood flow. *Computer Methods in Applied Mechanics and Engineering*, 316:646–667, 2017.

[19] H. Casquero, C. Bona-Casas, D. Toshniwal, T.J.R. Hughes, H. Gomez, and Y. Jessica Zhang. The divergence-conforming immersed boundary method: Application to vesicle and capsule dynamics. *Journal of Computational Physics*, 425:109872, 2021.

[20] D. Chapelle and A. Ferent. Modeling of the inclusion of a reinforcing sheet within a 3D medium. *Mathematical Models and Methods in Applied Sciences*, 13(04):573–595, 2003.

[21] Dominique Chapelle and Klaus-Jurgen Bathe. *The finite element analysis of shells - Fundamentals*. Springer Science & Business Media, 2010.

[22] Dominique Chapelle, Anca Ferent, and K.J. Bathe. 3D-shell elements and their underlying mathematical model. *Mathematical Models and Methods in Applied Sciences*, 14(1):105–142, 2004.

[23] Snorre H. Christiansen and Kaibo Hu. Generalized finite element systems for smooth differential forms and Stokes'problem. *Numerische Mathematik*, 140(2):327–371, 2018.

[24] Corti, Daniele C., Delay, Guillaume, Fernández, Miguel A., Vergnet, Fabien, and Vidrascu, Marina. Low-order fictitious domain method with enhanced mass conservation for an interface stokes problem. *ESAIM: Mathematical Modelling and Numerical Analysis*, 58(1):303–333, 2024.

[25] J. De Hart, G.W.M. Peters, P.J.G. Schreurs, and F.P.T. Baaijens. A three-dimensional computational analysis of fluid–structure interaction in the aortic valve. *Journal of Biomechanics*, 36(1):103–112, 2003.

[26] S. Deparis, M. Discacciati, G. Fourestey, and A. Quarteroni. Fluid-structure algorithms based on Steklov-Poincaré operators. *Computer Methods in Applied Mechanics and Engineering*, 195(41-43):5797–5812, 2006.

[27] J. Donea, S. Giuliani, and J.-P. Halleux. An arbitrary Lagrangian-Eulerian finite element method for transient dynamic fluid-structure interactions. *Computer Methods in Applied Mechanics and Engineering*, 33(1-3):689–723, 1982.

[28] M.A. Fernández and M. Moubachir. A Newton method using exact Jacobians for solving fluid-structure coupling. *Computers & Structures*, 83(2-3):127–142, 2005.

[29] L. Formaggia and F. Nobile. A stability analysis for the arbitrary Lagrangian Eulerian formulation with finite elements. *East-West Journal of Numerical Mathematics*, 7(2):105–131, 1999.

[30] K.J. Galvin, A. Linke, L.G. Rebholz, and N.E. Wilson. Stabilizing poor mass conservation in incompressible flow problems with large irrotational forcing and application to thermal convection. *Computer Methods in Applied Mechanics and Engineering*, 237/240:166–176, 2012.

[31] A. Gerstenberger and W. A. Wall. An extended finite element method/Lagrange multiplier based approach for fluid–structure interaction. *Computer Methods in Applied Mechanics and Engineering*, 197(19-20):1699–1714, 2008.

[32] A. J. Gil, A. Arranz Carreño, J. Bonet, and O. Hassan. An enhanced Immersed Structural Potential Method for fluid-structure interaction. *Journal of Computational Physics*, 250:178–205, 2013.

[33] B.E. Griffith and X. Luo. Hybrid finite difference/finite element immersed boundary method. *International Journal for Numerical Methods in Biomedical Engineering*, 33(12):e2888, 2017.

[34] Boyce E Griffith. Immersed boundary model of aortic heart valve dynamics with physiological driving and loading conditions. *International Journal for Numerical Methods in Biomedical Engineering*, 28(3):317–345, 2012.

[35] S. Groß and A. Reusken. An extended pressure finite element space for two-phase incompressible flows with surface tension. *Journal of Computational Physics*, 224(1):40–58, 2007.

[36] E. Hachem, S. Feghali, R. Codina, and T. Coupez. Immersed stress method for fluid-structure interaction using anisotropic mesh adaptation. *International Journal for Numerical Methods in Engineering*, 94(9):805–825, 2013.

[37] J. Haslinger and Y. Renard. A new fictitious domain approach inspired by the extended finite element method. *SIAM Journal on Numerical Analysis*, 47, 2009.

[38] C. Hesch, A. J. Gil, A. Arranz Carreño, and J. Bonet. On continuum immersed strategies for Fluid-Structure Interaction. *Computer Methods in Applied Mechanics and Engineering*, 247-248:51–64, 2012.

[39] Johan Hoffman, Johan Jansson, and Michael Stöckli. Unified continuum modeling of fluid-structure interaction. *Mathematical Models and Methods in Applied Sciences*, 21(03):491–513, 2011.

[40] Johan Jansson, Niyazi Cem Degirmenci, and Johan Hoffman. Adaptive unified continuum FEM modeling of a 3D FSI benchmark problem. *International journal for numerical methods in biomedical engineering*, 33(9):e2851, 2017.

[41] D. Kamensky, M.-C. Hsu, D. Schillinger, J. A. Evans, A. Aggarwal, Y. Bazilevs, M. S. Sacks, and T. J. R. Hughes. An immersogeometric variational framework for fluid–structure interaction: Application to bioprosthetic heart valves. *Computer Methods in Applied Mechanics and Engineering*, 284:1005–1053, 2015.

[42] T. Kenner. The measurement of blood density and its meaning. *Basic Research in Cardiology*, 84(2):111–124, 1989.

[43] Mikel Landajuela, Marina Vidrascu, Dominique Chapelle, and Miguel A Fernández. Coupling schemes for the FSI forward prediction challenge: comparative study and validation. *International journal for numerical methods in biomedical engineering*, 33(4):e2813, 2017.

[44] Phill-Seung Lee and Klaus-Jürgen Bathe. Development of MITC isotropic triangular shell finite elements. *Computers & Structures*, 82(11):945–962, 2004.

[45] Youngyu Lee, Phill-Seung Lee, and Klaus-Jürgen Bathe. The MITC3+ shell element and its performance. *Computers & Structures*, 138:12–23, 2014.

[46] Ju Liu and Alison L Marsden. A unified continuum and variational multiscale formulation for fluids, solids, and fluid–structure interaction. *Computer Methods in Applied Mechanics and Engineering*, 337:549–597, 2018.

[47] Y. Liu and W.K. Liu. Rheology of red blood cell aggregation by computer simulation. *Journal of Computational Physics*, 220(1):139–154, 2006.

[48] R.D. Mindlin. Influence of rotary inertia and shear on flexural motions of isotropic elastic plates. *Journal of Applied Mechanics*, 18:31–38, 1951.

[49] Rajat Mittal and Gianluca Iaccarino. Immersed boundary methods. *Annual Review of Fluid Mechanics*, 37(1):239–261, 2005.

[50] Philippe Moireau, Dominique Chapelle, and Patrick Tallec. Filtering for distributed mechanical systems using position measurements: Perspectives in medical imaging. *Inverse Problems*, 25:35010–25, 2009.

[51] T. Nakata and H. Liu. A fluid–structure interaction model of insect flight with flexible wings. *Journal of Computational Physics*, 231(4):1822–1847, 2012.

[52] T. Nomura and T.J.R. Hughes. An arbitray Lagrangian-Eulerian finite element method for interaction of fluid and rigid body. *Computer Methods in Applied Mechanics and Engineering*, 95(1):115–138, 1992.

[53] Charles S Peskin. The immersed boundary method. *Acta numerica*, 11:479–517, 2002.

[54] Charles S Peskin and Beth Feller Printz. Improved volume conservation in the computation of flows with immersed elastic boundaries. *Journal of Computational Physics*, 105(1):33–46, 1993.

[55] E. Reissner. The effect of transverse shear deformation on the bending of elastic plates. *Journal of Applied Mechanics*, 12(2):A69–A77, 1945.

[56] Robert Rosencranz and Steven Bogen. Clinical laboratory measurement of serum, plasma, and blood viscosity. *American journal of clinical pathology*, 125 Suppl:S78–86, 2006.

[57] S. Roy, L. Heltai, and F. Costanzo. Benchmarking the immersed finite element method for fluid-structure interaction problems. *Computers & Mathematics with Applications*, 69(10):1167–1188, 2015.

[58] T. Sawada and A. Tezuka. LLM and X-FEM based interface modeling of fluid-thin structure interactions on a non-interface-fitted mesh. *Computational Mechanics*, 48(3):319–332, 2011.

[59] P. Singh, D.D. Joseph, T.I. Hesla, R. Glowinski, and T.-W. Pan. A distributed Lagrange multiplier/fictitious domain method for viscoelastic particulate flows. *Journal of Non-Newtonian Fluid Mechanics*, 91(2):165–188, 2000.

[60] Keith Stein, Tayfun Tezduyar, and Richard Benney. Mesh moving techniques for fluid-structure interactions with large displacements. *Journal of Applied Mechanics*, 70(1):58–63, 2003.

[61] W. Strychalski and R. D. Guy. Intracellular pressure dynamics in blebbing cells. *Biophysical Journal*, 110(5):1168–1179, 2016.

[62] K. Takizawa and T. E. Tezduyar. Computational methods for parachute fluid–structure interactions. *Archives of Computational Methods in Engineering*, 19(1):125–169, 2012.

[63] K. Takizawa, T.E. Tezduyar, A. Buscher, and S. Asada. Space-time interface-tracking with topology change (ST-TC). *Computational Mechanics*, 54(4):955–971, 2014.

[64] Kenji Takizawa, Yuri Bazilevs, and Tayfun E Tezduyar. Space–time and ale-vms techniques for patient-specific cardiovascular fluid–structure interaction modeling. *Archives of Computational Methods in Engineering*, 19(2):171–225, 2012.

[65] Tayfun Tezduyar. Stabilized finite element formulations for incompressible flow computations. *Advances in Applied Mechanics*, 28:1–44, 1992.

[66] R. Van Loon, P. D. Anderson, F. P. T. Baaijens, and F. N. Van de Vosse. A three-dimensional fluid–structure interaction method for heart valve modelling. *Comptes Rendus Mécanique*, 333(12):856–866, 2005.

[67] X. Wang and L.T. Zhang. Interpolation functions in the immersed boundary and finite element methods. *Computational Mechanics*, 45(4):321–334, 2010.

[68] Xingshi Wang and Lucy T Zhang. Modified immersed finite element method for fully-coupled fluid–structure interactions. *Computer Methods in Applied Mechanics and Engineering*, 267:150–169, 2013.

[69] G. D. Weymouth, D. G. Dommermuth, K. Hendrickson, and D.K.P. Yue. Advancements in Cartesian-grid methods for computational ship hydrodynamics. In *26th Symposium on Naval Hydrodynamics (16/09/06-21/09/06)*, Rome, Italy, 2006.

[70] Thomas Wick. Flapping and contact FSI computations with the fluid–solid interface-tracking/interface-capturing technique and mesh adaptivity. *Computational Mechanics*, 53(1):29–43, 2014.

[71] Lucy Zhang, Axel Gerstenberger, Xiaodong Wang, and Wing Liu. Immersed finite element method. *Computer Methods in Applied Mechanics and Engineering*, 193:2051–2067, 2004.

[72] A. Zilian and A. Legay. The enriched space-time finite element method (EST) for simultaneous solution of fluid-structure interaction. *International Journal for Numerical Methods in Engineering*, 75(3):305–334, 2008.

[73] Stefano Zonca, Christian Vergara, and Luca Formaggia. An unfitted formulation for the interaction of an incompressible fluid with a thick structure via an XFEM/DG approach. *SIAM Journal on Scientific Computing*, 40(1):B59–B84, 2018.